Acta Pharmaceutica Sinica B 2025;15(10):5050−5070

Chinese Pharmaceutical Association
Institute of Materia Medica, Chinese Academy of Medical Sciences

Acta Pharmaceutica Sinica B

www.elsevier.com/locate/apsb
www.sciencedirect.com

ORIGINAL ARTICLE

PROTAC-loaded nanocapsules degrading BRD4 for radio-chemotherapy sensitization in glioblastoma

Yun Guo[a], Mingzhu Fang[a], Shilin Zhang[a], Zheng Zhou[a], Zonghua Tian[a], Haoyu You[a], Yun Chen[a], Jingyi Zhou[a], Xiaobao Yang[b], Yunke Bi[c,*], Chen Jiang[a,e,*], Tao Sun[a,d,*]

[a]*Key Laboratory of Smart Drug Delivery/Innovative Center for New Drug Development of Immune Inflammatory Diseases (Ministry of Education), Minhang Hospital, State Key Laboratory of Medical Neurobiology and MOE Frontiers Center for Brain Science, Department of Pharmaceutics, School of Pharmacy, Fudan University, Shanghai 201203, China*
[b]*Gluetacs Therapeutics (Shanghai) Co., Ltd., Shanghai 201306, China*
[c]*Department of Neurosurgery, Shanghai General Hospital, School of Medicine, Shanghai Jiaotong University, Shanghai 200025, China*
[d]*Quzhou Fudan Institute, Quzhou 324003, China*
[e]*Department of Digestive Diseases, National Regional Medical Center, Binhai Campus of the First Affiliated Hospital, Fujian Medical University, Fuzhou 350212, China*

Received 21 October 2024; received in revised form 20 January 2025; accepted 10 February 2025

KEY WORDS

Glioblastoma;
PROTAC;
Nanocapsules;
DNA damage repair;
Radiotherapy;
Nanosensitizer;
BRD4;
GSH responsive

Abstract Glioblastoma (GBM) is a highly aggressive primary brain tumor characterized by poor prognosis. Conventional chemo-radiotherapy demonstrates limited therapeutic efficacy and is often accompanied by significant side effects, largely due to factors such as drug resistance, radiation resistance, the presence of the blood−brain barrier (BBB), and the activation of DNA damage repair mechanisms. There is a pressing need to enhance treatment efficacy, with BRD4 identified as a promising target for increasing GBM sensitivity to therapy. Lacking small molecule inhibitors, BRD4 can be degraded using PROteolysis Targeting Chimera (PROTAC), thereby inhibiting DNA damage repair. To deliver PROTAC, SIAIS171142 (SIS) effectively, we designed a responsive nanocapsule, $MPL_{(SS)}P$@SIS, featuring GBM-targeting and GSH-responsive drug release. Modified with 1-methyl-L-tryptophan (MLT), nanocapsules facilitate targeted delivery of SIS, downregulating BRD4 and sensitizing GBM cells to radiotherapy

This article is part of a special issue entitled: Targeted Radiopharmaceuticals published in Acta Pharmaceutica Sinica B.
*Corresponding authors.
E-mail addresses: doctorbyk@163.com (Yunke Bi), jiangchen@shmu.edu.cn (Chen Jiang), sunt@fudan.edu.cn (Tao Sun).
Peer review under the responsibility of Chinese Pharmaceutical Association and Institute of Materia Medica, Chinese Academy of Medical Sciences.

https://doi.org/10.1016/j.apsb.2025.03.018

and chemotherapy. After intravenous administration, $MPL_{(SS)}P$@SIS selectively accumulates in tumor tissue, enhancing the effects of radiotherapy and temozolomide (TMZ) by increasing DNA damage and oxidative stress. GSH activates the nanocapsules, triggering BRD4 degradation and hindering DNA repair. In mouse models, the nanosensitizer, combined with TMZ and X-ray irradiation, efficiently inhibited the growth of GBM. These findings demonstrate a novel PROTAC-based sensitization strategy targeting BRD4, offering a promising approach for effective GBM therapy.

1. Introduction

Glioblastoma (GBM) is the most aggressive and prevalent primary brain tumor, characterized by a dismal prognosis, short survival times, high recurrence rates, and significant treatment challenges[1,2]. Current standard-of-care radio-chemotherapy offers limited efficacy and substantial side effects due to several factors: inherent drug and radiotherapy (RT) resistance, poor penetration of therapeutic drugs across the blood−brain barrier (BBB) and blood-tumor barrier (BTB), and the inherent toxicity of high-dose RT[3,4]. Consequently, long-term survival benefits remain elusive for most GBM patients despite treatment modalities such as surgery, radiotherapy, and chemotherapy[5]. Furthermore, a strong correlation exists between GBM stress resistance and poor patient outcomes, highlighting the urgent need for novel therapeutic strategies[6]. Both radiotherapy and chemotherapy, including TMZ and X-ray, induce DNA damage and thus inhibit the growth of tumor cells[7-9].

However, following radio-chemotherapy, DNA damage repair pathways are activated, prompting the cell to initiate emergency DNA repair mechanisms to preserve its normal functions[10,11]. While DNA damage is the crucial point of current clinical treatment[12], DNA damage repair exerts a crucial function in the resistance encountered during the treatment of GBM. By performing this role, it safeguards the stability of the intracellular environment[13]. In tumors, RT could induce lethal DNA damage[14], but tumor cells enhance DNA damage repair mechanisms by upregulating proteins associated with homologous recombination repair, such as RAD51 and RAD51-associated protein 1 (RAD51AP1)[15,16]. This response ultimately reduces the sensitivity of tumor cells to RT. Recently, as a key transcriptional regulator involved in DNA damage repair, bromodomain-containing protein 4 (BRD4) has been regarded as a promising target to sensitize malignant GBM to RT[17].

As a member of the BET family, BRD4 recognizes histone acetylation marks, thereby promoting gene transcription and influencing physiological processes such as the cell cycle, proliferation, and apoptosis[18-20]. BRD4 is essential for GBM development and is considered one of the core driving genes of this malignancy[21]. Consequently, inhibiting BRD4 has been proposed as an epigenetic strategy to combat GBM[22,23]. However, BRD4 is often regarded as an undruggable target due to the absence of effective small molecule inhibitors[24]. This situation necessitates the exploration of novel therapeutic approaches for BRD4 that extend beyond traditional small molecule inhibitors[25]. In contrast to small molecules, proteolysis-targeting chimeras (PROTACs) facilitate the degradation of the protein of interest (POI) *via* the ubiquitin−proteasome system in a catalytic manner[26]. PROTACs can effectively degrade BRD4, addressing significant limitations such as drug resistance associated with conventional small molecule inhibitors by completely degrading the target protein at a low dose[27,28].

Despite the potential, current PROTAC molecules lack tumor selectivity, resulting in the degradation of the POI in normal tissues and leading to severe side effects[29]. Therefore, developing effective strategies for tumor-specific POI degradation to enhance radio-chemotherapy remains a significant challenge[30,31]. This nanoplatform presents a promising strategy for effective drug delivery while minimizing systemic toxicity, thereby providing a reference point for the treatment of malignant tumors[32]. Nanodrug delivery systems offer a viable approach to enhance the efficacy of PROTACs[33]. Given their excellent biocompatibility and controllability[34-36], nanocapsule-based biomedical platforms show great potential in PROTAC delivery, potentially prolonging systemic circulation, reducing rapid clearance, and facilitating targeted delivery to GBM[37].

Herein, we developed a novel nanosensitizer therapeutic strategy using PROTAC-included nanocapsules. These nanocapsules are composed of biocompatible PEG-pLys-pPhe polymers and the PROTAC, SIAIS171142 (SIS), which degrades the BRD4 protein. Meanwhile, MLT modification enables targeted delivery to GBM tumor[38,39]. The nanocapsules enhance DNA damage by mediating ubiquitin−proteasome-dependent degradation of BRD4, an undruggable target protein, thereby inhibiting DNA damage repair (Scheme 1). Furthermore, these versatile nanocapsules decrease glutathione (GSH) levels and disrupt the original redox balance within the tumor microenvironment, thereby promoting an increase in reactive oxygen species (ROS) levels, which are the key mediators of DNA damage[40]. This approach enhances DNA damage in GBM during radio-chemotherapy. This study demonstrates the promising potential of combining PROTAC-based therapy with GBM radio-chemotherapy, suggesting that inhibiting DNA damage repair is a beneficial strategy for tumor treatment.

2. Materials and methods

2.1. Synthesis and characterizations of the polymers

The chemical structure of SIS is shown in the Supporting Information Fig. S1. In the chemical synthesis process, the specific procedures are clearly illustrated in Supporting Information Figs. S2 and S3. To ensure the accuracy and integrity of the characterizations, all synthesized products underwent analysis using ^1H NMR spectra with a frequency of 400 MHz (Oxford Instruments, Abingdon, UK). The entire synthesis process and related details regarding every synthesis step are meticulously laid out in the Supporting Information

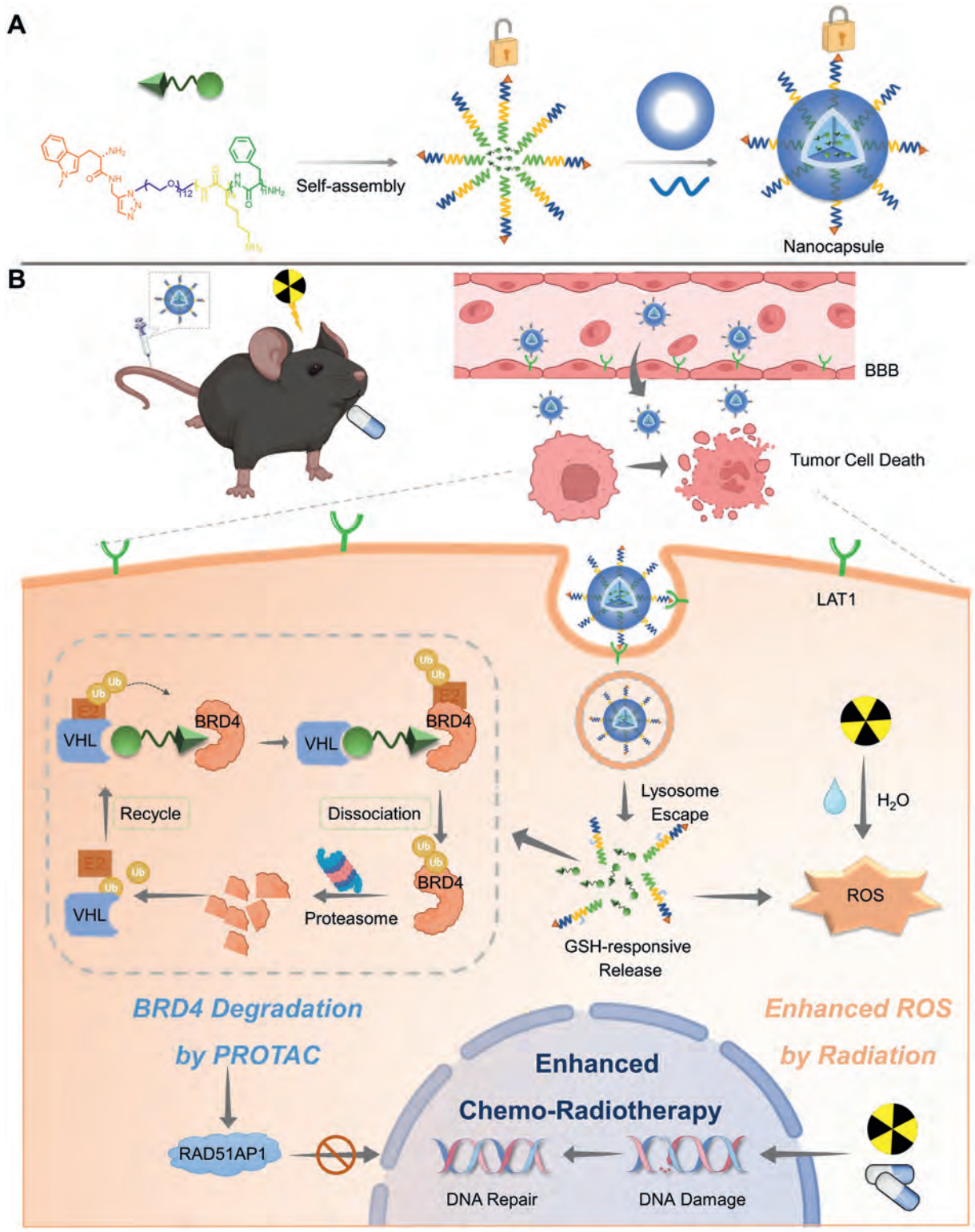

Scheme 1 Schematic of $MPL_{(SS)}P$@SIS nanocapsules for GBM treatment combined with radio-chemotherapy. (A) Synthesis of $MPL_{(SS)}P$@SIS nanocapsules. (B) Enhanced anti-GBM effects induced by $MPL_{(SS)}P$@SIS nanocapsules after intravenous injection to GBM-bearing mice with radio-chemotherapy.

2.2. Preparation and characterizations of $MPL_{(SS)}P$@SIS nanocapsules

Triblock polymers were dissolved in dimethyl sulfoxide (DMSO) to form a solution. Nanocapsules were prepared using the nanoprecipitation method by first preparing DMSO solutions of $mPEG_{112}$-pLys-pPhe-CH_3, MLT-PEG_{112}-pLys-pPhe-NH_2, and SIS, each at a concentration of 20 mg/mL. The DMSO solutions (220 μL) of $mPEG_{112}$-pLys-pPhe-CH_3, MLT-PEG_{112}-pLys-pPhe-NH_2, and SIS were then mixed up. This mixture was subsequently added dropwise into deionized water while stirring on constant turbulence for 2 h. Following this, the solution was dialyzed (3500 MWCO, ThermoFisher Scientific, Waltham, MA, USA) for 12 h to remove DMSO, with water being replaced every 4 h, resulting in the formation of MPLP@SIS nanoparticles (NPs).

To create the $MPL_{(SS)}P$@SIS nanocapsules, the 3,3′-dithiobis (sulfosuccinimidyl propionate) (DTSSP) solution was added to the MPLP@SIS formulation and allowed to react at 37 °C for 6 h. The product was then subjected to dialysis for 12 h to remove any excess DTSSP, yielding the final $MPL_{(SS)}P$@SIS nanocapsules. Four kinds of NPs, empty NPs (PLP), empty nanocapsules ($PL_{(SS)}P$), drug-loaded NPs (PLP@SIS), and drug-loaded nanocapsules ($PL_{(SS)}P$@SIS), were designed and prepared. They were all made by nanoprecipitation. In the experimental procedure, before further analysis, all the prepared liquids were filtered using a 0.22 μm membrane (Whatman, Maidstone, UK).

The characterization process involved the measurement of key parameters such as the NP size distribution, polydispersity index (PDI), and zeta potential, which were determined using a dynamic light scattering (DLS) machine (Zetasizer Nano-ZS, Malvern Panalytical, Malvern, UK). Additionally, to gain a visual understanding of the morphological characteristics of the various NPs, transmission electron microscopy (TEM) was carried out.

Pyrene molecules were utilized as a fluorescence probe to ascertain the critical micelle concentration (CMC) of NPs. Initially, NP solutions were diluted to various concentrations based on material calculations. Following this, 999 μL of each NP dilution was combined with 1 μL of a pyrene acetone solution (0.1 mmol/L) and incubated at 37 °C for 2 h. Fluorescence intensity was then recorded at 372 nm using a microplate reader from BioTek Instruments (Winooski, VT, USA). The intensity data were graphed against NP concentrations, and linear regression analysis was employed to discern two separate linear regions. The CMC was established as the x-coordinate where these two lines intersect.

To assess the *in vitro* stability of NPs, three independent samples ($n = 3$) of the NP formulation were prepared. Each preparation was diluted in phosphate-buffered saline (PBS, pH = 7.4) and maintained at 37 °C with continuous stirring at 60 rpm. Samples were collected daily over 7 days for DLS measurements to monitor changes in particle size and distribution. A certain amount of $MPL_{(SS)}P$@SIS solution was mixed with an equal-volume DMEM solution containing 20% fetal bovine serum (FBS) and then stored at 4 °C. Subsequently, the particle size and PDI of the NPs were measured by DLS for seven consecutive days.

2.3. Drug loading efficiency

To assess the drug loading efficiency (DLE) and encapsulation efficiency (EE) of the NPs, the lyophilized powder of the NPs was first weighed and subsequently dissolved in acetonitrile. The concentration of the SIS was then measured using a high-performance liquid chromatography (HPLC, Agilent Technologies, Santa Clara, CA, USA) method. DLE and EE of NPs were calculated with the following Eqs. (1) and (2):

$$\text{DLE (\%)} = (\text{Weight of SIS encapsulated in NP} / \text{Weight of NP}) \times 100 \quad (1)$$

$$\text{EE (\%)} = (\text{Weight of SIS encapsulated in NP} / \text{Total SIS}) \times 100 \quad (2)$$

Total SIS means the total mass of SIS involved in the preparation of NPs.

The HPLC method was carried out using specific parameters. An Agilent C18 column, with a length of 250 mm and an inner diameter of 4.6 mm, was utilized for the separation process. The mobile phase, which is crucial for the elution of analytes, is designated as a flow rate of 0.6 mL/min and was composed of a mixture of 70% acetonitrile and 30% H_2O (*v*/*v*), with the addition of 0.1% *v*/*v* trifluoroacetic acid to enhance the separation efficiency and peak shape. The injection volume of the sample was carefully set at 10 μL. A diode array detector (DAD) was used for the detection with a scan wavelength of 220 nm.

2.4. In vitro GSH-sensitive transformation and drug release characterization

The sensitivity of nanocapsules to GSH was assessed using 10 mmol/L dithiothreitol (DTT), which simulated elevated GSH levels in an intertumoral environment. To confirm the GSH sensitivity of the nanocapsules, $PL_{(SS)}P$@SIS was diluted in phosphate-buffered saline (PBS, pH 7.4) containing DTT and incubated at 37 °C for 4 h. Following incubation, the changes in particle size of the nanocapsules were analyzed using a particle size analyzer, and TEM was measured.

The release kinetics of SIS from the NPs was monitored over 12 h *in vitro*. Specifically, 1.5 mL of the solution was placed into dialysis bags (3500 MWCO) suspended in a 15-mL centrifuge tube filled with release buffer while shaking at 80 rpm at 37 °C. To maintain the sink conditions, the 15-mL centrifuge tube was PBS (pH 7.4, 0.1% Tween 80, 13.5 mL). The GSH-sensitive release was assessed in the presence of DTT (10 μmol/L and 10 mmol/L, respectively). At the specific time point (0.5, 1, 1.5, 2, 3, 4, 5, 7, and 12 h), 100 μL solution was collected from the external dialysis bags in the centrifuge tube. Simultaneously, an equal volume of fresh release buffer was added to ensure the total volume remained consistent. The concentration of released SIS was then determined using the HPLC method as before.

2.5. Cellular uptake and internalization mechanism

Cell lines G422 and G422/Luc (Tongpai Biotech, Shanghai, China) were grown in Dulbecco's modified Eagle's medium (DMEM) enriched with 10% FBS, 10 U/mL penicillin, and 10 μg/mL streptomycin. The cultures were kept at 37 °C in a humidified environment with 5% CO_2.

Near-infrared probe Cyanine 5 (Cy5) was linked to the free amino groups of PEG-pLys-pPhe polymer for tracking the fate of nanocapsules. The reaction condition was to avoid light and react at room temperature, and the target product was obtained after dialysis treatment.

G422s were seeded in 12-well plates (cell density: 1×10^5 cells per well). When reaching a confluence of 80%−90%, the DMEM was removed, and cultured cells were washed twice with PBS 7.4. Then Cy5-labeled nanocapsules with different modifications of MLT (0, 10, 20, 40, 80, and 100%) were added. After incubation for 0.5, 1, or 2 h, the cells were washed three times with Hank's Balanced Salt Solution (HBSS) to remove NPs that were not taken up by cells. Specifically, non-targeted nanocapsules ($PL_{(SS)}P$@Cy5) were further evaluated by the same procedure.

The cells were subsequently visualized using a fluorescence microscope (CKX53, Olympus, Osaka, Japan). Furthermore, cells from parallel samples were removed from the plate for analysis with a flow cytometer (cytoFLEX, Beckman Coulter, Indianapolis, IN, USA).

To evaluate the internalization mechanism of GBM, the G422 cells were then incubated under different inhibitive conditions, which were HBSS supplemented with colchicine (2 μg/mL), chlorpromazine (CPZ, 2 μg/mL), filipin (2 μg/mL) or excess MLT (100 μg/mL) for 30 min. Then, $MPL_{(SS)}P$@Cy5 was added and incubated with G422s for 1 h at 37 or 4 °C, respectively. Then, the cells were washed three times with HBSS and then collected into HBSS. Finally, the uptake of nanocapsules in G422s was also measured by flow cytometry.

To further explore the internalization process, G422 cells were seeded in confocal culture dishes (Corning, Corning, NY, USA). All cells were incubated with Cy5-labeled nanocapsules (10% modification degree of MLT) for 15, 30, 60, and 120 min and then washed with HBSS twice.

Then, to localize the nuclei and late endosomes/lysosomes, all the cells were incubated with Hoechst 33342 (ThermoFisher Scientific, Waltham, MA, USA) at a concentration of 1 μg/mL and LysoTracker Deep Redat (ThermoFisher Scientific, Waltham, MA, USA) at a concentration of 50 nmol/L for 30 min. Following immunofluorescence staining, all cells were measured using a 63 × oil immersion objective lens of a confocal fluorescence microscope (Carl Zeiss AG, Oberkochen, Germany).

2.6. *In vitro BBB model construction and integrity assay*

BCEC monolayer in a transwell system was established as the *in vitro* BBB model. First, the cellular uptake of BCECs was investigated. BCECs were seeded in 12-well plates (2×10^5 cells per well), and upon reaching 80%−90% confluence, the DMEM medium was removed, and the cultured cells were washed twice. $PL_{(SS)}P$@Cy5 and $MPL_{(SS)}P$@Cy5 were then added at equal concentrations of Cy5. After incubation for 1 h, upon the removal of NPs that were not internalized by the cells, the cells were washed three times with HBSS. To specifically examine the role of MLT in cellular uptake, BCECs were pre-treated with an excess of MLT, followed by incubation with $MPL_{(SS)}P$@Cy5. The results were analyzed using flow cytometry.

To assess the permeability of nanocapsules across the BBB, brain microvascular endothelial cells (BCECs) were plated in a 3 μm Transwell insert (NEST, Wuxi, China) at a density of 1.5×10^4 cells per well. After approximately 20 days, the cells were treated with various samples placed beneath the inserts. FITC-labeled dextran (4 kDa) was employed as a permeability indicator and was added alongside the nanocapsules. The cells were incubated at 37 °C, with 50 μL samples collected at 5, 10, 15, 30, and 60 min for dextran analysis while replenishing the same volume of fresh medium.

The concentration of Cy5 (Ex = 640 nm, Em = 670 nm) was quantified using a microplate reader (BioTek Instruments, Winooski, VT, USA), as was the concentration of FITC-labeled dextran (Ex = 483 nm, Em = 520 nm). The apparent permeability coefficients (P_{app}) were calculated using the following Eq. (3):

$$P_{app} = (dQ/dt) / (C_0 \times S) \quad (3)$$

dQ/dt is the permeability rate (nmol/s), C_0 denotes the initial concentration (nmol/mL) in the Transwell insert, and S indicates the membrane area (0.33 cm^2) of the insert.

2.7. *The study on cytotoxic effect and apoptosis of nanocapsules*

2.7.1. *Cell viability assay*

To evaluate the susceptibility of the GBM cell lines G422 to different drugs, the cell viability assay was conducted. G422 cells were seeded in 96-well culture plates at a density of 2×10^3 cells/well. After reaching 60%−70% confluence, the cells were incubated with different concentrations of drugs or preparations in DMEM. After incubation for 24 or 48 h, the medium was removed, and cells were washed three times with HBSS. Then, 10 μL per well Cell Counting Kit-8 (CCK-8) solution (10%, *v/v*, Meilunbio, Dalian, China) was added to the well at 37 °C for 2 h. The absorbance was read with the microplate reader (BioTek Instruments, Winooski, VT, USA) at 540 nm. Besides, the cells without treatment were considered as control, and cell viability was calculated based on the normalized absorbance.

2.7.2. *Apoptosis detection*

Firstly, G422 cells were seeded in a 12-well plate with a density of 4×10^4 per well. After reaching a 60%−70% confluence, the cells were incubated with different treatments for 48 h. Single cells were obtained by 0.25% trypsin without EDTA, stained with an apoptosis detection kit (Meilunbio, Dalian, China), incubated for 20 min, and measured by the flow cytometry (cytoFLEX, Beckman Coulter, Brea, CA, USA).

2.8. *GSH depletion and ROS measurement in tumor cells*

To analyze intracellular GSH and ROS in cells, G422s were seeded into 6-well plates at a density of 1×10^5 cells per well first. When reaching a 60%−70% confluence, various treatments were administered to the cells for a period of 24 h respectively. After that, the G422 cells were collected using 0.25% trypsin−EDTA and resuspended in HBSS. The depletion of GSH was analyzed using the Reduced glutathione assay kit (Jiancheng Biotechnology, Nanjing, China).

Furthermore, the ROS level of G422s was detected using the ROS probe (Beyotime Biotechnology, Shanghai, China), and the detection results were then measured by flow cytometry (cytoFLEX, Beckman Coulter, Indianapolis, IN, USA).

2.9. *Confocal microscopy of G422s in vitro*

The G422s with different treatments were washed with HBSS three times, fixed with 4% formaldehyde for 20 min, and further stained with 4′,6-diamidino-2- phenylindole (DAPI) for 10 min. The treated G422s were subjected to a confocal fluorescence microscope (IX2-RFACA, Olympus, Osaka, Japan) for analysis. Finally, the statistics were quantified using the ImageJ software.

2.10. In vivo distribution and brain-targeting efficiency

The G422 orthotopic glioblastoma model was utilized to investigate the distribution of nanocapsules *in vivo*. The mice received intravenous injections of various nanocapsules at an equivalent dose of Cy5. After 24 h, the mice were anesthetized and perfused with a 4% paraformaldehyde (PFA) fixative solution (Servicebio, Wuhan, China), followed by photographing the fluorescence intensity of the isolated tissues. Following dehydration, tumor tissues embedded in optimal cutting temperature compound were sectioned (Leica, CM1900, Wetzlar, Germany). Subsequently, these tumor sections were stained with DAPI for analysis and then photographed *via* confocal laser scanning microscopy (CLSM, Leica TCS-SP8 STED, Wetzlar, Germany).

2.11. In vivo anti-tumor efficacy study

2.11.1. Animals and establishment of the GBM model mice

C57BL/6 male mice (19−23 g) were procured from the Department of Experimental Animals at Fudan University and housed under standardized laboratory conditions. All animal handling procedures were conducted in accordance with the guidelines approved by the Institutional Animal Care and Use Committee of China. To establish a GBM model, male C57BL/6 mice weighing between 19 and 23 g underwent intracranial injection of G422/Luc cells. Specifically, 2×10^5 G422/Luc cells suspended in 5 μL of HBSS were injected into the striatum at coordinates 1.8 mm lateral to the bregma and 3 mm deep. A brain stereotactic apparatus was employed to ensure accurate tumor placement. The incidence of GBM in this model was observed to be 85%.

2.11.2. Animal experimental design

After GBM model construction, the animals were randomly divided into 7 groups ($n = 6$). $MPL_{(SS)}P@SIS$ was injected through the tail vein at a dose of SIS = 0.2 mg/kg every two days for five times. The dose of TMZ was 20 mg/kg, administered by oral gavage. At the same time, the X-ray was 4 Gy for 5 min every time.

The Amptek Mini-X X-Ray Tube (Precision X-ray, MA, USA) was used for the treatment of experimental solutions, cells, and animals. The Amptek Mini-X X-Ray Tube was set at 50 kV and 80 μA. To improve the peak to background ratio for elements of interest, 3 mil Cu and 1 mil Ag were used as the Filters on an X-ray tube.

2.11.3. Assay of antitumor efficacy

After treatment, tumor signal and survival rate were under observation. Mice were visualized under the IVIS® imaging system (Caliper PerkinElmer, Waltham, MA, USA) at Ex/Em = 633/660 nm after anesthesia. After different treatments, the brains and major organs of each group were excised and fixed in 4% PFA. The apoptotic cells in GBM were stained with cleaved caspase-3 antibody, while the proliferating cells were stained with Ki67 antibody. Histological changes in major organs and brains were stained with hematoxylin and eosin (H&E), and then the stained sections were analyzed using a fluorescence microscope (Olympus, Tokyo, Japan). Finally, the statistics were analyzed using the ImageJ software (National Institutes of Health, Bethesda, USA).

Immunofluorescence staining of tumor tissue: tumor tissue samples were snap-frozen following dehydration with a sucrose solution. Subsequently, the frozen tissues were sectioned, and sections were then stained with various primary antibodies and incubated overnight at 4 °C. Fluorescently labeled secondary antibodies (goat anti-rabbit IgG, ThermoFisher Scientific, Waltham, MA, USA) were applied after this incubation. The stained sections were photographed using confocal microscopy to assess the localization and expression of different proteins. Additionally, the statistics were analyzed using the ImageJ software.

2.12. Western blot procedure

Cell samples were lysed in radioimmunoprecipitation assay (RIPA) lysis buffer supplemented with phenylmethanesulfonyl fluoride (1 mmol/L). The lysing process involved ultrasound treatment at 40% power within an ice water bath for 10 s, which was carried out three times with 10-s intervals in between. After lysis, the resultant supernatant containing the extracted proteins was collected through centrifugation at 13,000 rpm for 10 min at 4 °C (ThermoFisher Scientific, Waltham, MA, USA). The protein concentration in the cell samples was determined using a BCA Protein Assay Kit (Beyotime Biotechnology, Shanghai, China). For subsequent analysis, total protein samples (10 μg per well) underwent separation *via* SDS-PAGE electrophoresis, initially at a voltage of 80 V for 30 min, followed by a transition to 120 V for a duration of 2 h. In contrast, tissue samples were utilized at a concentration of 20 μg per well. The proteins were then transferred to polyvinylidene fluoride (PVDF) membranes, and then the PVDF membranes were blocked with 5% fat-free milk for 2 h. Primary antibodies were incubated overnight at 4 °C, with details of the antibodies used for Western blot (WB) provided in Supporting Information Table S1. After the primary incubation, membranes were washed three times, each for 10 min, using TBST buffer. Following these washes, membranes were subjected to incubation with horseradish peroxidase (HRP)-conjugated secondary antibodies (anti-rabbit or anti-mouse antibody) at a dilution of 1:1000 (*v*/*v*) for 1.5 h. Additional washing with TBST buffer (pH = 7.4) was performed three times for 10 min each. Protein expression levels were detected employing enhanced chemiluminescence (ECL) autoradiography with ECL plus reagent. Quantitative analysis of the WB images was carried out utilizing ImageJ software, with all gray value statistics documented in the manuscript.

2.13. Statistical analysis

Statistical evaluations were conducted using GraphPad Prism v.9.4.1. Comparisons between groups were analyzed through *t*-tests or one-way ANOVA, with a significance threshold set at $P < 0.05$. Data are expressed as means ± standard deviation (SD), where $^*P < 0.05$, $^{**}P < 0.01$, and $^{***}P < 0.001$ indicate statistically significant differences.

3. Results and discussion

3.1. The synthesis and characterizations of the synthetic polymers

The amphiphilic triblock polymer, $mPEG_{112}$-pLys-pPhe-CH_3, was synthesized, and the comprehensive and specific steps are clearly illustrated in Supporting Information Fig. S2. The utilization of $mPEG_{112}$-NH_2 as a macroinitiator for the ring-opening polymerization of NCA monomers is a crucial aspect. The subsequent chemical modifications, namely the acetylation of the polymeric terminal amino and the deprotection of Cbz, are integral parts of

the overall synthetic strategy[41]. The confirmation of the chemical composition through ^{1}H NMR spectroscopy provides reliable evidence of the molecular structure and composition of the NCA monomers and intermediate polymers (Supporting Information Fig. S4−S9). Moreover, the verification of successful polymerization *via* the reduced elution time in gel permeation chromatography (GPC) results further validates the effectiveness of the synthesis process.

For specific GBM targeting, MLT-PEG$_{112}$-pLys-pPhe-NH$_2$ was synthesized and the detailed synthetic routes are illustrated in Supporting Information Fig. S3. Firstly, in order to protect the active amino group of the MLT, MLT reacted with di-*tert*-butyl decarbonate ((Boc)$_2$O) to obtain *Nα*-(tert-butoxycarbonyl)-1-methyl-L-tryptophan (1-MLT-Boc). Then, the MLT(Boc)-propargyl was synthesized *via* amidation of 1-MLT-Boc with amine groups on propargylamine. Subsequently, the MLT(Boc)-Propargyl was attached to the azide end of N$_3$-PEG$_{112}$-NH$_2$ through a click reaction, followed by ring-opening polymerization of activated NCA monomers using MLT(Boc)-PEG$_{112}$-NH$_2$ as macroinitiators and the removal of Cbz chemical group to obtain MLT-PEG$_{112}$-pLys$_{12}$-pPhe$_{16}$-NH$_2$. The chemical composition of 1-MLT-Boc, MLT(Boc)-propargyl, MLT(Boc)-PEG$_{112}$-NH$_2$, and intermediate polymers was verified through ^{1}H NMR spectroscopy (Supporting Information Fig. S10−S14). Additionally, the reduced elution time of GPC results also confirmed the successful synthesis of the polymer (Supporting Information Fig. S15).

Moreover, the CMC of the polymers was detected, including mPEG$_{112}$-pLys$_{12}$-pPhe$_{16}$-CH$_3$ and mPEG$_{112}$-pLys$_{12}$-pPhe$_{13}$-CH$_3$. The CMC of NPs comprised of mPEG$_{112}$-pLys$_{12}$-pPhe$_{16}$-CH$_3$ was approximately 223.24 μg/mL, whereas that of mPEG$_{112}$-pLys$_{12}$-pPhe$_{13}$-CH$_3$ exhibited a higher CMC of about 416.09 μg/mL (Supporting Information Fig. S16). Therefore, mPEG$_{112}$-pLys$_{12}$-pPhe$_{16}$-CH$_3$ was consequently selected to construct the nanocapsules and enhance the stability against dilution by bodily fluids.

3.2. *Preparation and characterizations of the multifunctional nanocapsules*

The SIS-loaded nanocapsule (MPL$_{(SS)}$P@SIS) was prepared *via* nanoprecipitation method and disulfide bond cross-linking reaction (Fig. 1A). In brief, the DMSO solution of mPEG$_{112}$-pLys$_{12}$-pPhe$_{16}$-CH$_3$, MLT-PEG$_{112}$-pLys$_{12}$-pPhe$_{16}$-NH$_2$ and SIS were mixed according to a certain mass ratio (9:1:1) in aqueous solution/PBS under mild stirring at room temperature. The redundant DMSO was removed *via* dialysis, and then the MPLP@SIS NPs were

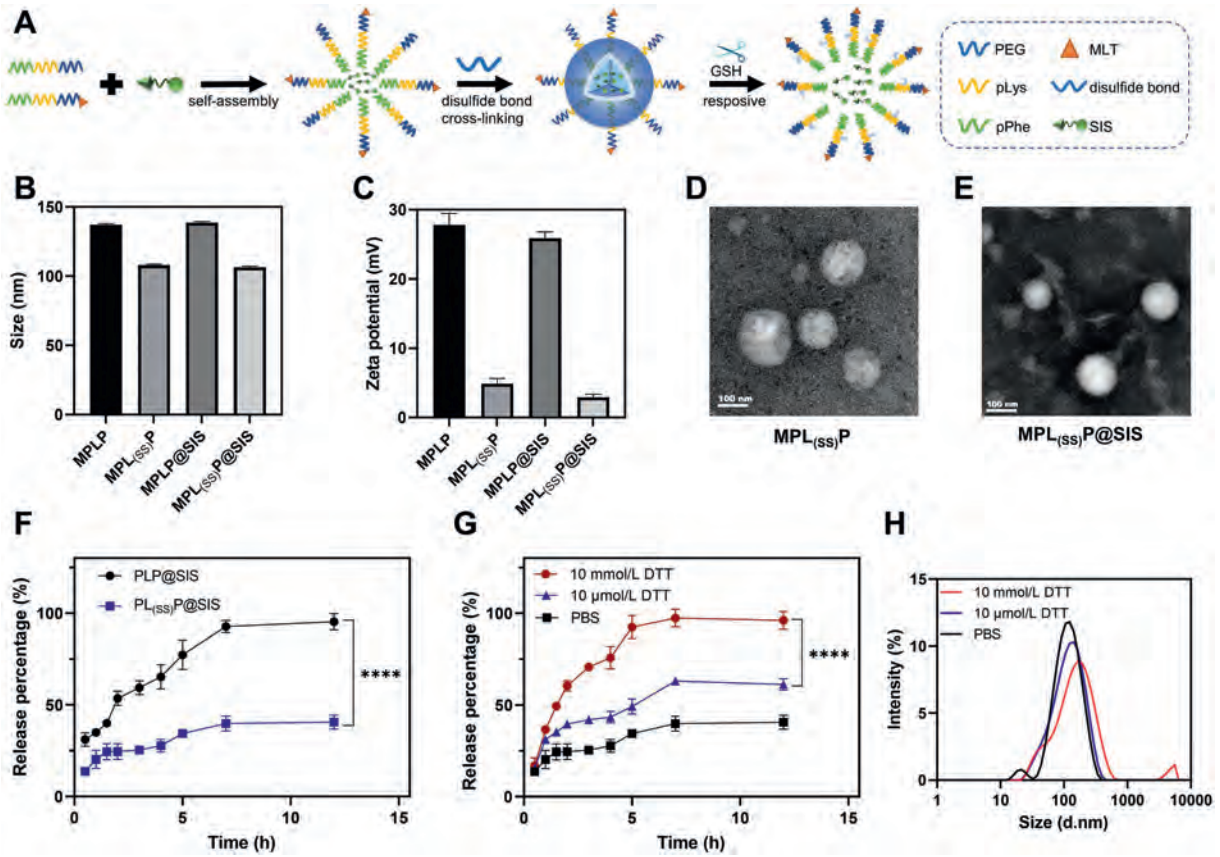

Figure 1 Characterizations of MPL$_{(SS)}$P@SIS nanocapsules. (A) Illustration of the preparation process for MPL$_{(SS)}$P@SIS *via* nanoprecipitation and disulfide bond cross-linking, along with the responsive mechanism under GSH stimulation. (B) Particle size and (C) zeta potential of various NPs (n = 3). (D−E) Representative TEM images of MPL$_{(SS)}$P nanocapsules (D) and MPL$_{(SS)}$P@SIS nanocapsules (E) (scale bar = 100 nm). (F) SIS release profile of PLP@SIS and PL$_{(SS)}$P@SIS in PBS (pH 7.4) (n = 3). (G) SIS release profile of PL$_{(SS)}$P@SIS nanocapsules in PBS (pH 7.4) with or without DTT (10 μmol/L and 10 mmol/L, respectively) (n = 3). (H) Alterations in the size distribution of PL$_{(SS)}$P@SIS nanocapsules after incubation with DTT for 4 h (10 μmol/L and 10 mmol/L, respectively). Data are presented as mean ± SD. *P < 0.05. ns, not significant.

attained. Then, to entitle the preparation with greater stability and bio-responsiveness, DTSSP, which is a cleavable crosslinker, was selected to react with the MPLP@SIS NPs. Subsequently, the GSH-sensitive nanocapsules were synthesized, which contained the PROTAC in the hydrophobic core. In the same manner, MPLP and $MPL_{(SS)}P$ were prepared without the load of SIS.

DLS and zeta potential were measured among different NPs (Fig. 1B and C, Supporting Information Table S2). There was no significant difference between empty nanocapsules and SIS-loaded nanocapsules. However, the particle size of $MPL_{(SS)}P$@SIS declined to about 106 nm, smaller than that of MPLP@SIS (138 nm), due to the denser core of nanocapsules. Meanwhile, the zeta potential of $MPL_{(SS)}P$@SIS (2.9 mV) was decreased after the cross-linking reaction, and the neutral charge was beneficial to the bio-safety of nanocapsules, avoiding clearance by the reticuloendothelial system *in vivo* upon the systemic administration. Moreover, consistent with the DLS, similar results were observed from the TEM images (Fig. 1D and E). The $MPL_{(SS)}P$@SIS nanocapsules showed a continuous and amorphous appearance, with a diameter around 100 nm. In addition, the hydrodynamic diameter and PDI of $PL_{(SS)}P$@SIS and $MPL_{(SS)}P$@SIS demonstrated stability (Supporting Information Figs. S17 and S18). Notably, the DLS of PLP@SIS had changed, indicating that the cross-linking strategy could enhance the stability of the nanocapsules.

To investigate the encapsulation ability of SIS, the calibration curve of SIAIS171142 was detected with HPLC (Supporting Information Fig. S19). The DLE and EE were presented in Table S2, and $MPL_{(SS)}P$@SIS nanocapsules exhibited a DLE of approximately 7% and an EE of 63.74%.

Since the targeting moiety, as a small molecule, does not significantly affect the properties of the NPs, non-targeted nanocapsules were employed to investigate the stability, drug release, and other characteristics *in vitro*. Subsequently, the *in vitro* release profile of SIS was examined. *In vitro* release studies revealed that PLP@SIS NPs exhibited a relatively faster release rate, with approximately 75% of SIS released within the initial 5 h under PBS conditions (Fig. 1F). Conversely, the release rate of SIS from the $PL_{(SS)}P$@SIS nanocapsules was slower, with only about 30% of the drug released in the first 5 h, suggesting that cross-linking markedly enhanced the stability of nanocapsules and reduced non-specific drug release. Additionally, the tumor-sensitive release of SIS is crucial in GBM therapy. The crosslinking characteristics of the GSH-sensitive compound DTSSP enable the nanocapsules to disintegrate selectively within the tumor microenvironment, facilitating a swift release of their therapeutic payload. Simultaneously, GSH can be effectively scavenged through interaction with DTT. Additionally, the release of SIS, prompted by GSH, was observed in PBS containing DTT (Fig. 1G).

Moreover, upon exposure to 10 mmol/L DTT, drug release from $PL_{(SS)}P$@SIS nanocapsules was significantly accelerated, showing a similar release behavior to that of PLP@SIS in PBS (pH 7.4), indicating that $PL_{(SS)}P$@SIS nanocapsules can rapidly release SIS in response to DTT. To verify the responsiveness of the cross-linker and nanocapsules to GSH, the diameter changes of $MPL_{(SS)}P$@SIS incubated with DTT were further tested. In addition, a significant particle size increase was observed (Fig. 1H, Supporting Information Table S3). Comparable results were also witnessed in the TEM images (Supporting Information Fig. S20), probably due to the breakdown of the $MPL_{(SS)}P$@SIS structure.

3.3. Investigation of cellular uptake, transcytosis, and brain-targeting ability

To achieve the brain-targeting function, receptor- and transporter-mediated targeting strategies have been widely used in the targeted therapy of brain glioma[42,43]. To target and accumulate nanocapsules in GBM, especially the tumor core, a Trp analogue MLT was modified as a targeting ligand. Upon binding with L-type amino transporter 1 (LAT1), the nanocapsules could penetrate the brain parenchyma *via* the BBB. As tumor cells need more Trp, the nanocapsules were enriched in the tumor core microenvironment and then taken up by the tumor cells[44-46].

Firstly, G422 cells were selected to simulate GBM tumor cells. According to relevant literature, LAT1 is abundantly expressed in the tumor cells as a typical membrane protein[47]. Considering that our strategy of cellular uptake transcytosis of tumor cells is based on LAT1, as shown in Fig. 2A, the expression of LAT1 was first detected on GBM tumor cells. As shown in Fig. 2B and Supporting Information Fig. S21, we have observed and confirmed the expression of LAT1 membrane protein on the GBM tumor cells of G422 and GL261 by WB. Meanwhile, flow cytometry was also used to detect the LAT1 membrane protein on the surface of four different cells (Supporting Information Fig. S22), and the relative quantitative results also showed that the GBM tumor cells of G422 and GL261 expressed more LAT1 membrane protein (Supporting Information Fig. S23). Then, a monolayer model was constructed in Transwell inserts to simulate the BBB *in vitro* using BCEC cells (Fig. 2C).

Near-infrared probe Cyanine 5 (Cy5) was linked to the free amino groups of PEG-pLys-pPhe polymer for tracking the fate of nanocapsules *in vitro* and *in vivo*. The concentration of Cy5 in the nanoparticles was determined according to its standard curve (Supporting Information Fig. S24). Cy5-labeled nanocapsules exhibited similar size and PDI to $MPL_{(SS)}P$@SIS nanocapsules (Supporting Information Table S4), enabling their use as a suitable surrogate for tracking distribution in cells and animals. To analyze the binding affinity of MLT to LAT1, the Cy5-labeled nanocapsules ($MPL_{(SS)}P$@Cy5) with different MLT modification proportions were prepared.

As illustrated in Fig. 2D and E, the Cy5-labeled nanocapsules were incubated with G422s for 0.5 h, and the fluorescence signal was afterward quantitatively analyzed by flow cytometry, where the results suggested that MLT modification could significantly enhance the cellular uptake of nanocapsules in G422s compared with the control group. In addition, according to the quantified results of cellular uptake, the nanocapsules with a 10% MLT-modification ratio had the strongest uptake property (Fig. 2F). It's worthwhile noting that the maximum binding rate was also achieved by 10% ligand modification after the fluorescent-labeled nanocapsules were incubated with tumor cells for both 1 and 2 h (Supporting Information Fig. S25, Supporting Information Table S5). Therefore, the 10% modification ratio was finally selected as the subsequent targeted nanocapsules.

Then, the mechanism of cellular uptake was explored in G422 cells. Specifically speaking, G422s were preincubated with different uptake inhibitors and then treated with $MPL_{(SS)}P$@Cy5, nontargeted nanocapsules ($PL_{(SS)}P$@Cy5), or a mixture of $MPL_{(SS)}P$@Cy5 and excess MLT, respectively. We compared the uptake of fluorescent-labeled nanocapsules in each group (Fig. 2G and H). Firstly, the uptake of $MPL_{(SS)}P$@Cy5 was significantly higher than that of $PL_{(SS)}P$@Cy5. The low temperature of 4 °C, along with colchicine and CPZ, had inhibitory effects on the uptake of G422 cells, indicating that $MPL_{(SS)}P$@Cy5 nanocapsules

are primarily internalized through energy-dependent mechanisms, specifically caveolin-mediated and macropinocytosis-mediated endocytosis. This finding is consistent with the LAT1-mediated uptake mechanisms described in reported literatures[38,48,49].

Furthermore, excessive MLT markedly inhibited cellular uptake, highlighting the essential role of LAT1-mediated transcytosis in the internalization process. Previous studies have shown that the internalization of nanopreparations leads to the formation of macropinosomes[50], a specialized type of early endosome, which subsequently allows these preparations to evade lysosomal degradation *via* the circulating endosome pathway[49]. To explore this mechanism, LysoTracker Green was employed to label the endosomes and lysosomes within G422 cells[51,52], enabling us to assess the intracellular distribution of $MPL_{(SS)}P$@Cy5 nanocapsules.

After a 15 min incubation with the nanocapsules, yellow signals indicative of colocalization between the green and red signals were detected by us, suggesting a substantial accumulation of nanocapsules within endosomes or lysosomes. However, as the incubation time extended to 30, 60, and 120 min, the yellow colocalization signals diminished. By the 120 min mark, a predominance of distinct green and red signals was observed, with only a few yellow signals remaining (Fig. 2I, Supporting Information Fig. S26). This change suggests that the nanocapsules successfully escaped from the endosomal or lysosomal compartments.

Next, brain capillary endothelial cells (BCECs) were selected to simulate the BBB *in vitro*[53], enabling the investigation of the brain-targeting capabilities of the nanocapsules at the cellular level. LAT1 has been documented to be a characteristic membrane protein that is abundantly expressed at the BBB[54]. Given that MLT-mediated penetration across the BBB relies on LAT1, the protein expression of LAT1 in brain endothelial cells (bEnd.3) was first evaluated using WB analysis (Fig. S21). In addition, cellular uptake was evaluated by flow cytometry on BCECs. As illustrated in Fig. 2J, fluorescence signals were quantitatively measured across different treatment groups. Compared to $PL_{(SS)}P$@Cy5 or a mixture of $MPL_{(SS)}P$@Cy5 with excess MLT, the higher fluorescence signal observed for $MPL_{(SS)}P$@Cy5 indicated that BCECs internalized more targeted nanocapsules modified with MLT.

After culturing BCEC cells in the monolayer model for 20 days, the nanocapsules were administered to the upper compartment of the Transwell inserts, and the fluorescence intensity in the lower compartment was measured to evaluate permeability efficiency, expressed as P_{app} values at different time points. The results demonstrated that $MPL_{(SS)}P$@Cy5 exhibited the highest permeability among the tested groups (Fig. 2K). Notably, the permeability decreased in the group where $MPL_{(SS)}P$@Cy5 was mixed with excessive MLT, suggesting that MLT-based modification, in conjunction with LAT1-mediated transcytosis, facilitates the passage of nanocapsules across the BBB. Additionally, the P_{app} values of FITC-labeled dextran (4 kDa) were measured both before and after the experiment (Fig. 2L), with the calibration curve of FITC-labeled dextran (Supporting Information Fig. S27). These values were consistent with those reported in other studies utilizing monolayer cell models[55]. The results indicated that the preparation did not compromise the integrity of the BBB and that the monolayer cell models met the criteria for *in vitro* BBB simulation before and after the experiments.

3.4. *In vitro anti-tumor effects*

We first verified the degradation ability of the PROTAC, SIAIS171142 (SIS), since it is a new compound (Fig. S1) that has not been reported previously. Similar to the mechanism of the PROTAC (Fig. 3A), SIS can effectively degrade the BRD4 protein *via* the ubiquitin−proteasome system (Fig. 3B). The direct tumor-killing capacity on G422 cells was assessed using the CCK-8. As shown in Fig. 3C and D, the final preparation, $MPL_{(SS)}P$@SIS nanocapsules exhibited higher cytotoxicity (IC_{50} = 157.8 nmol/L) compared to free SIS (IC_{50} = 489.8 nmol/L). The preparation without the MLT ($PL_{(SS)}P$@SIS) demonstrated lower cytotoxicity than the final preparation, indicating that MLT modification enhances toxicity to tumor cells (Fig. 3D).

Additionally, G422 cells were selected to simulate GBM tumor cells and to investigate cellular safety. The results showed that the survival rate of G422 cells exceeded 80% (Supporting Information Fig. S28) when the concentration reached 100 μg/mL. Notably, the cellular safety of empty nanocapsules improved after the cross-linking reaction, which contributed to a decreased zeta potential. Considering the LAT1 expression in normal brain parenchymal cells, the cytotoxicity in normal brain parenchymal cells bEnd.3 was also evaluated (Supporting Information Fig. S29). A significant level of toxicity was only induced at a relatively high concentration of 400 nmol/L that would not approach the threshold because of the high degradation activity. The tumor-killing capacity was further validated among different groups over 48 h (Fig. 3E) at a concentration of SIS (200 nmol/L), similar to the tumor-killing capacity observed at 24 h (Supporting Information Fig. S30). The cytotoxicity of $MPL_{(SS)}P$@SIS nanocapsules was higher than that of free SIS and $PL_{(SS)}P$@SIS, demonstrating that intracellular self-assembled nanocapsules can enhance cytotoxicity as a means of drug delivery.

Furthermore, the BRD4 degradation properties of both SIS and $MPL_{(SS)}P$@SIS nanocapsules were investigated using WB analysis. SIS efficiently degraded the POI at a maximal degradation concentration of 400 nmol/L in G422 tumor cells *in vitro* (Fig. 3B). In contrast, the $MPL_{(SS)}P$@SIS nanocapsules demonstrated enhanced POI degradation capacity, achieving maximal degradation at a concentration of 100 nmol/L (Fig. 3F and G, Supporting Information Fig. S31), while the $PL_{(SS)}P$@SIS nanocapsules reached a maximal degradation concentration of 200 nmol/L (Supporting Information Fig. S32). This difference was primarily attributed to MLT-mediated cell uptake, which allowed the nanocapsules to specifically target G422 cells and improve efficacy. Interestingly, the Hook effect was observed in the WB results exclusively by PROTAC, as PROTACs tend to show the Hook effect at a higher concentration: an effective PROTAC typically reduces the POI levels dose-dependently to a certain concentration, while the POI may gradually increase beyond the point, showing a bell-shaped dose−response curve[27]. This is consistent with the mechanism of PROTAC. A high concentration of PROTAC favors the formation of E3-PROTAC and PROTAC-POI binary complexes, while the POI-PROTAC-E3 ternary complex is depleted, showing a decreased degradation activity[56].

BRD4 plays a crucial role in transcription regulation in cancer[21], and inhibition of BRD4 can pharmacologically modulate Myc transcriptional function[57,58], contributing to the pathogenesis of many cancers. We observed higher expression of BRD4 in GBM cells (G422 and GL261) compared to normal cells (HEK293 and bEnd.3) (Supporting Information Fig. S33). *In vivo*, there are also differences in the expression of BRD4 in tumor tissues and normal tissues of GBM mouse models, and the expression level of BRD4 in tumor tissues is higher than that in normal tissues (Supporting Information Fig. S34). This reflects the importance of BRD4 in tumorigenesis and development to some extent. To test whether

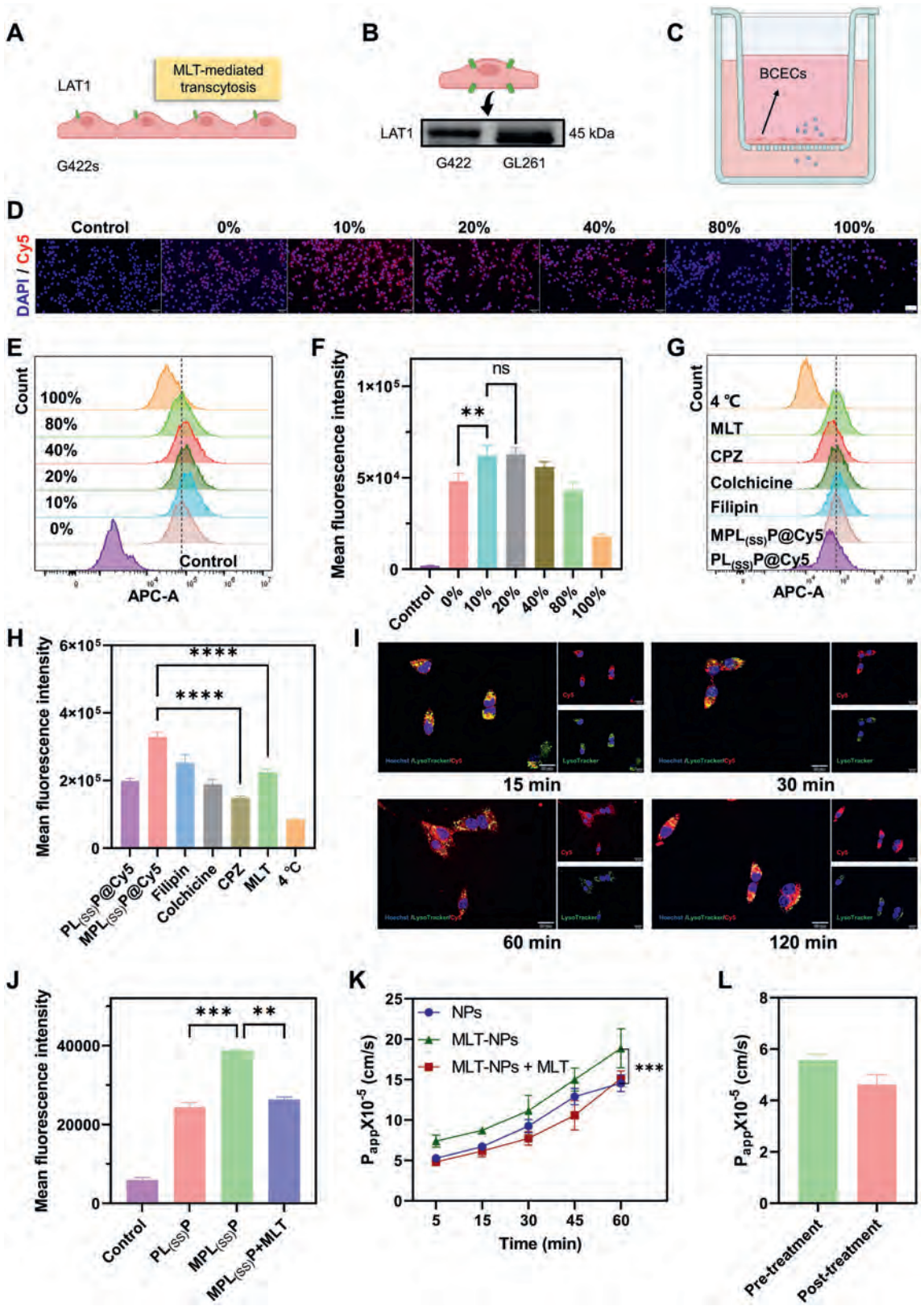

Figure 2 Investigation of the mechanisms of cellular uptake, transcytosis, and brain-targeting ability. (A) Mechanism of cellular uptake of the nanocapsules by G422 cells. (B) Measurement of LAT1 membrane proteins in GBM cells (G422 and GL261) *via* WB. (C) Illustration of the construction of a BBB model *in vitro*. (D) Cellular uptake of Cy5-labeled nanocapsules with varying MLT-modification ratios in G422 cells (red: Cy5-labeled nanocapsules; blue: DAPI; scale bar = 50 μm). (E) Flow cytometry analysis of cellular uptake in G422 cells with different MLT-modification ratios. (F) Quantification of results from (E) (n = 3). (G) Flow cytometry analysis of cellular uptake in G422 cells with various

BRD4 inhibition specifically abrogates Myc-dependent transcription, WB analysis was utilized to examine the expression of BRD4 and c-Myc (Fig. 3H). As illustrated in Fig. 3B and I, $MPL_{(SS)}P$@SIS nanocapsules were identified as reducing c-Myc expression by SIS targeting the expressed BRD4.

According to previous studies, Bcl-2 and caspase-3 are key markers of cell apoptosis signaling pathways[59,60]. The specific mechanisms of apoptosis were further explored, and the expression of several signaling molecules in apoptosis-related pathways was also analyzed in differently treated cells (Fig. 3J). The WB results indicated that compared with the control groups, the SIS and $MPL_{(SS)}P$@SIS treatment groups led to decreased levels of Bcl-2 and caspase-3, while $MPL_{(SS)}P$ remained unchanged, suggesting that $MPL_{(SS)}P$@SIS promoted cell apoptosis.

Additionally, the apoptosis induced by SIS and $MPL_{(SS)}P$@SIS nanocapsules was investigated. The 7-AAD/Annexin-V staining assay demonstrated that SIS induced cell apoptosis (Supporting Information Fig. S35), as shown by flow cytometry. In contrast, $MPL_{(SS)}P$@SIS nanocapsules resulted in significant apoptosis in G422 cells (Fig. 3K). Overall, these results confirm that $MPL_{(SS)}P$@SIS effectively degrades BRD4 proteins and promotes cell apoptosis.

3.5. In vitro nanocapsules enhancing DNA damage and breaking BRD4−RAD51AP1 axis

RT can eliminate tumor cells by causing lethal DNA damage. However, RT upregulates the DNA homologous repair-associated protein, promoting DNA damage repair and decreasing the sensitivity of RT. To be precise, according to relevant literature, RT could upregulate the BRD4−RAD51AP1 axis (Fig. 4A), thereby reducing the sensitivity in GBM cells to X-ray irradiation[15,16].

It is widely accepted that γ-H2AX proteins are markers of DNA double-strand breaks[61]. The relationship between BRD4 degradation and DNA damage was then investigated, with γ-H2AX being used to assess the extent of DNA damage in G422 cells. As shown in Fig. 4B, SIS enhanced the expression of γ-H2AX, indicating that SIS increased DNA damage in G422 cells. As expected, $MPL_{(SS)}P$@SIS nanocapsules caused more severe DNA damage and exhibited higher levels of γ-H2AX expression compared to the other groups (Fig. 4C). Subsequent immunofluorescence staining further supported this conclusion, as illustrated in Fig. 4D. The γ-H2AX immunofluorescence assay was conducted to monitor the DNA double-strand break repair capacity in GBM cancer cells (G422) following different treatments. Consistent with the WB results, immunostaining of DNA damage markers confirmed that the most significant DNA damage occurred in G422 cells treated with $MPL_{(SS)}P$@SIS (Fig. 4D and E).

Herein, firstly, GBM cells had RAD51AP1 upregulation *in vitro* (Supporting Information Fig. S36), which was consistent with BRD4 expression (Fig. S33). Furthermore, similar to BRD4, the PROTAC and $MPL_{(SS)}P$@SIS nanocapsules both downregulated RAD51AP1 in a dose-dependent way *in vitro*, according to the WB assays (Fig. 4F and G).

Then, whether SIS could synergistically inhibit GBM cell growth combined with TMZ was further explored. In addition, the cytotoxicity of TMZ on G422 was also studied (Supporting Information Fig. S37). G422 cells were subjected to treatment with the indicated concentrations of TMZ and SIS, and the assessment of cell growth inhibition was carried out using the CCK-8 assay (Fig. 4H, Supporting Information Fig. S38). According to the outcomes of cell viability, the combination index (CI) scores were calculated to evaluate the combined effect of TMZ and SIS in GBM cells (Fig. 4I). Based on the literature[62], effects were categorized based on the CI values as follows: a CI greater than 1.25 was classified as antagonistic, a CI ranging from 0.75 to 1.25 was considered additive, and a CI less than 0.75 indicated synergistic effects. For example, the combination of TMZ at a concentration of 500 μmol/L and SIS at 2500 nmol/L might produce a stronger synergistic effect (CI = 0.17) with a relatively low cell viability of approximately 28.01%. When G422 cells were treated with TMZ at a concentration of 2000 μmol/L and SIS at 12,500 nmol/L, they exhibited an additive effect (CI = 1.07) with a cell viability of approximately 32.40%. In summary, these results demonstrated that SIS and TMZ show synergistic effects at most of the indicated concentrations.

3.6. In vitro enhanced cellular DNA damage combined with radio-chemotherapy

The above experimental results indicated that X-ray irradiation alone did not significantly alter BRD4 protein expression levels (Fig. 5A, Supporting Information Fig. S39), and only the nanocapsule $MPL_{(SS)}P$@SIS containing PROTAC in the 4 and 5 groups was able to downregulate BRD4 expression. Therefore, the underlying mechanisms were investigated by which the nanocapsules exert their sensitizing effects in the combined radiochemotherapy. As shown in Fig. 5B, the generation of ROS during RT is primarily attributed to the ionization of water molecules, which produces highly reactive hydroxyl radicals[63]. These radicals can then interact with DNA, leading to its damage. Furthermore, RT can also disrupt mitochondrial function, leading to increased ROS production[64]. In conclusion, ROS plays a crucial role in the therapeutic efficacy of high-energy radiation therapy. While their generation contributes to DNA damage and cell death, they also activate signaling pathways that can enhance the therapeutic effect of RT[40]. Understanding the complex interplay between ROS and RT is crucial for optimizing treatment strategies and minimizing side effects. Therefore, the main component of redox balance was measured, which refers to the equilibrium between ROS and antioxidants in the body.

As illustrated in Fig. 5C, the targeted nanocapsule group, $MPL_{(SS)}P$@SIS exhibited a significantly improved capacity for GSH depletion compared to the other groups. Treatment with $MPL_{(SS)}P$@SIS resulted in a significant increase in intracellular ROS levels (Fig. 5D). This observation is consistent with the established redox balance between ROS (oxidants) and GSH (antioxidant). The nanocapsule-mediated depletion of GSH

inhibitory conditions. (H) Quantification of results from (G) ($n = 3$). (I) Representative images of cellular uptake in G422 cells after incubation with $MPL_{(SS)}P$@Cy5 for 15, 30, 60, and 120 min (red: Cy5; blue: Hoechst; green: LysoTracker; scale bar = 20 μm). (J) Quantitative analysis of cellular uptake of the nanocapsules in BCECs by flow cytometry under different conditions ($PL_{(SS)}P$ = $PL_{(SS)}P$@Cy5, $MPL_{(SS)}P$ = $MPL_{(SS)}P$@Cy5, $n = 3$). (K) Quantitative transcytosis of $MPL_{(SS)}P$@Cy5 nanocapsules across the BBB model ($n = 3$). (L) Quantitative transcytosis of FITC-labeled dextran across the BBB model before and after treatment *in vitro* ($n = 3$). Data are presented as mean ± SD. $^*P < 0.05$. ns, not significant.

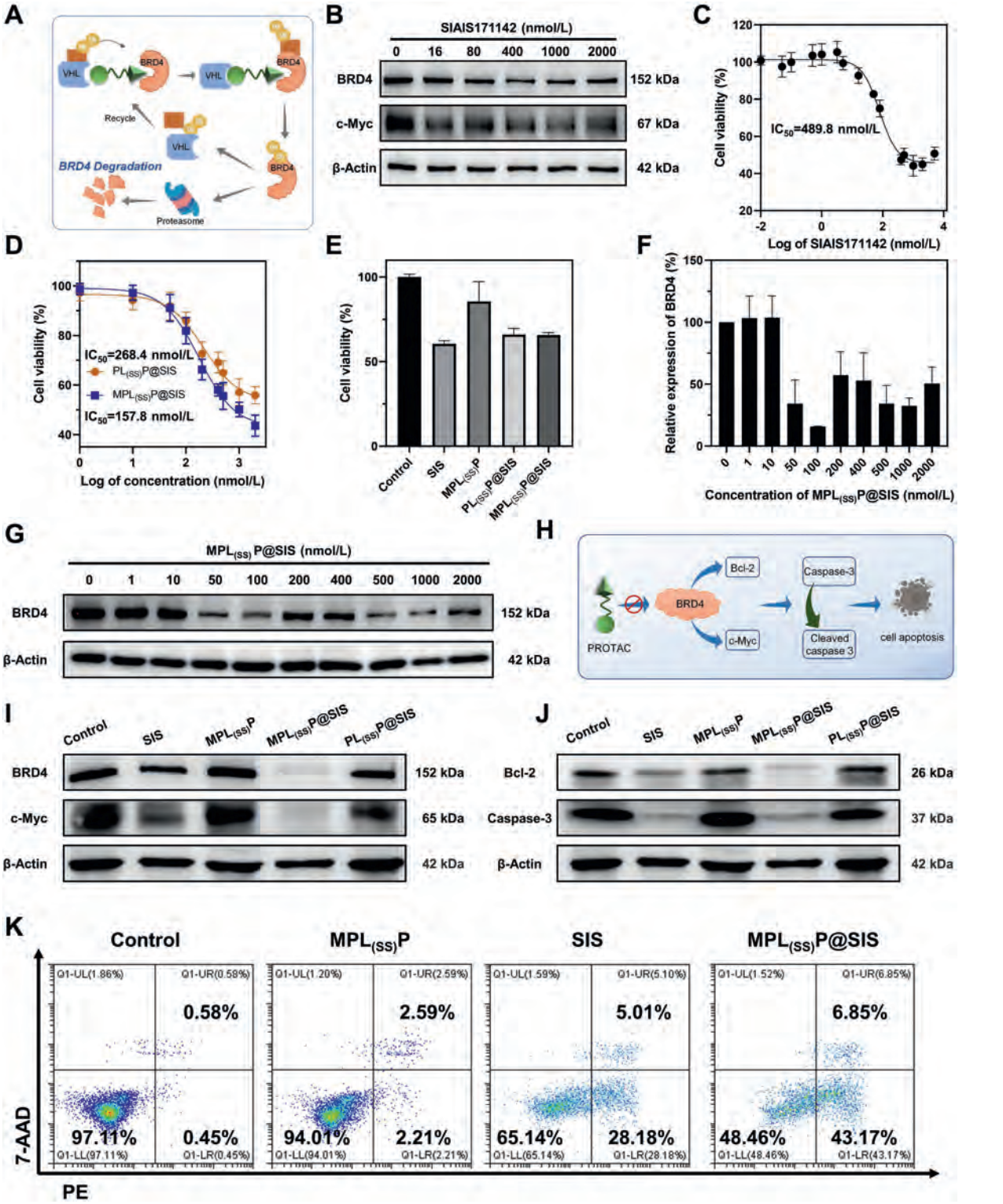

Figure 3 *In vitro* anti-tumor effects of $MPL_{(SS)}P$@SIS nanocapsules. (A) Schematic illustration of protein degradation *via* PROTAC. (B) WB analysis of BRD4 and c-Myc expression in G422 cells treated with various concentrations of SIS for 24 h. (C) Cell viability assay in G422 cells treated with different concentrations of SIS for 48 h ($n = 6$). (D) Cell viability assay in G422 cells treated with various concentrations of $PL_{(SS)}P$@SIS and $MPL_{(SS)}P$@SIS nanocapsules for 48 h ($n = 3$). (E) Cell viability assay in G422 cells treated with different groups for 48 h ($n = 3$). (F) Quantitative analysis of BRD4 expression in G422 cells treated with various concentrations of $MPL_{(SS)}P$@SIS nanocapsules for 24 h ($n = 3$). (G) WB analysis of BRD4 expression in G422 cells treated with different concentrations of $MPL_{(SS)}P$@SIS nanocapsules for 24 h. (I and J are the same protein samples and have the same internal reference protein β-actin.) (H) Schematic illustration of the nanocapsule-mediated cell apoptosis signaling pathway *via* BRD4 degradation. (I) WB analysis of BRD4 and c-Myc expression in G422 cells treated with different groups. (J) WB analysis of Bcl-2 and caspase-3 expression in G422 cells treated with different groups. (K) Flow cytometry analysis images of cell apoptosis using PE/7-AAD staining. Data are presented as mean ± SD. $^*P < 0.05$. ns, not significant.

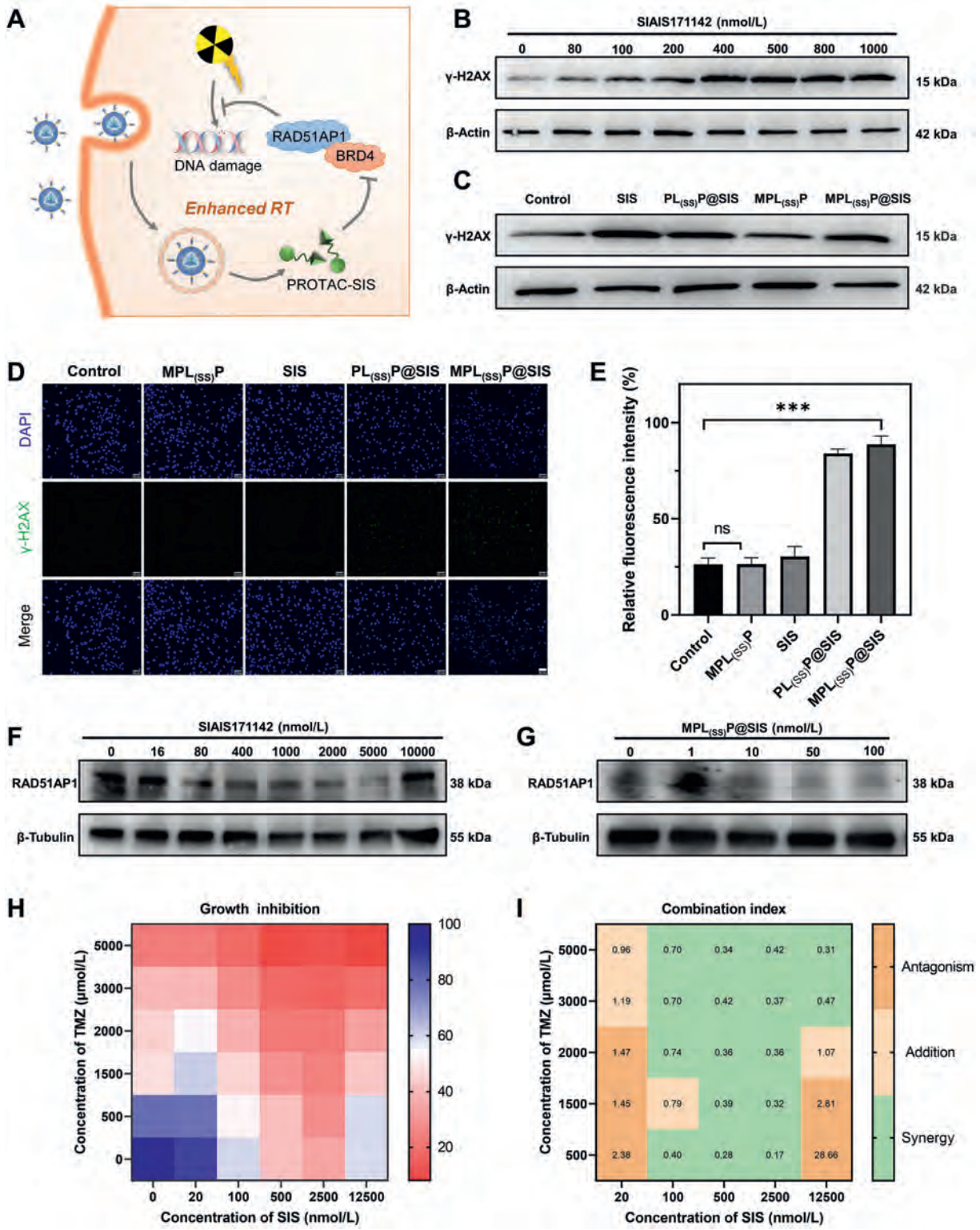

Figure 4 Nanocapsules breaking BRD4−RAD51AP1 axis to enhance RT and synergistic effect of TMZ in combination with SIS. (A) Schematic diagram illustrating how PROTAC-integrated nanocapsules disrupt the BRD4−RAD51AP1 axis to enhance RT. (B) WB analysis of γ-H2AX in G422 tumor cells treated with SIAIS171142 at different concentrations. (C) WB analysis of γ-H2AX in G422 tumor cells subjected to various treatments. (D) Immunostaining of DNA damage markers in G422 cells treated with different groups (green: γ-H2AX; blue: DAPI; scale bar = 50 μm). (E) Relative fluorescence intensity of (D). (F) WB analysis of RAD51AP1 downregulation in G422 tumor cells treated with SIS at different concentrations. (G) WB analysis of RAD51AP1 downregulation in G422 cells treated with $MPL_{(SS)}P$@SIS nanocapsules at different concentrations. (H) Cell growth inhibition of G422 cells following different treatments ($n = 3$). (I) Combination index (CI) scores of cells treated with TMZ in combination with SIS at different concentrations. Data are presented as mean ± SD. $^*P < 0.05$. ns, not significant.

disrupts this equilibrium, leading to elevated ROS levels and increased oxidative stress. To further investigate the impact of X-ray irradiation, we examined ROS levels following various treatment regimens. As shown in Fig. 5E, combined TMZ and X-ray radiotherapy alone induced a notable increase in intracellular ROS compared to the control group. Importantly, the addition of $MPL_{(SS)}P$@SIS nanocapsules further augmented ROS production under combined radio-chemotherapy conditions. The finding highlights the superior efficacy of the targeted nanocapsules in reducing intracellular GSH levels, potentially enhancing the effectiveness of radio-chemotherapy by enhancing DNA damage.

To assess the cytotoxic effects of $MPL_{(SS)}P$@SIS nanocapsules at the cellular level, the cell viability was evaluated after 48 h treatment of various conditions combined with X-ray. The results demonstrated that the addition of nanocapsules significantly enhanced cytotoxicity compared to X-ray + TMZ treatment alone, indicating a radio-sensitizing and chemosensitizing effect (Fig. 5F). DNA is the critical target in radiotherapy. X-ray irradiation and TMZ chemotherapy induce both single and double-strand DNA breaks, which is deadly. To verify the therapeutic efficacy of $MPL_{(SS)}P$@SIS further, γ-H2AX and DAPI fluorescent staining were used in experiments. It was observed that the DNA damage markers of tumor cells decreased in the combined group, suggesting that in the $MPL_{(SS)}P$@SIS + X-ray + TMZ group, most G422 cells were stained with green color, and their DNA was mostly damaged. In contrast, when treated with the X-ray plus TMZ, cells exhibited lower green fluorescence than the $MPL_{(SS)}P$@SIS + X-ray + TMZ group (Fig. 5G and H). The results indicate that the combination of $MPL_{(SS)}P$@SIS, X-ray, and TMZ blocked the DNA protective damage repair induced by BRD4. Therefore, $MPL_{(SS)}P$@SIS had the best therapeutic efficacy and represented an outstanding anti-tumor outcome under X-ray irradiation and TMZ chemotherapy.

3.7. *In vivo targeting ability of Cy5-labeled nanocapsules*

To assess the *in vivo* tumor-targeting efficacy and BBB penetration of $MPL_{(SS)}P$@Cy5 nanocapsules, an orthotopic GBM mouse model was employed. Cy5-labeled $MPL_{(SS)}P$ nanocapsules (MPS@C) and control $PL_{(SS)}P$ nanocapsules (PS@C, lacking the MLT targeting moiety) were intravenously administered to GBM-bearing mice. Non-invasive *in vivo* fluorescence imaging using an IVIS Spectrum system was performed at various time points post-injection (1−24 h) to monitor the biodistribution of the nanocapsules (Fig. 6A). As illustrated in Fig. 6B, MPS@C exhibited significantly higher fluorescence intensity at the GBM tumor site compared to PS@C throughout the observation period.

To further quantify the biodistribution, major organs (heart, liver, spleen, lung, and kidney) (Fig. 6C) and brains (Supporting Information Fig. S40) were harvested at 24 h post-injection for *ex vivo* fluorescence imaging. Quantitative analysis of the fluorescence signals revealed a statistically significant reduction in liver accumulation for the MLT-modified MPS@C nanocapsules compared to the unmodified PS@C nanocapsules (Fig. 6D), indicating improved tumor-specificity.

CLSM was used to visualize the distribution of MPS@C within tumor tissue sections. Moreover, CLSM images (Fig. 6E) revealed a significantly greater concentration of MPS@C fluorescence signal within both the core and satellite regions of the GBM tumors compared to control groups, further supporting the efficient tumor penetration and targeted accumulation of the MLT-modified nanocapsules. Furthermore, the fluorescence intensity within the brains was approximately threefold higher for MPS@C compared to PS@C (Fig. 6F), demonstrating the enhanced tumor targeting and BBB penetration afforded by the MLT modification. These findings collectively demonstrate that the incorporation of MLT imparts significant tumor-targeting capabilities to the nanocapsules, enabling enhanced accumulation within GBM tumors and improved penetration across the BBB.

3.8. *In vivo therapeutic efficacy of $MPL_{(SS)}P$@SIS*

The *in vivo* anti-tumor efficacy of $MPL_{(SS)}P$@SIS was explored in G422/Luc GBM-bearing mice, which were categorized into seven groups: saline, $MPL_{(SS)}P$@SIS, X-ray + TMZ, $MPL_{(SS)}P$@SIS + TMZ, $MPL_{(SS)}P$@SIS + X-ray, $PL_{(SS)}P$@SIS + X-ray + TMZ, and $MPL_{(SS)}P$@SIS + X-ray + TMZ (Fig. 7A). In the course of treatment, as revealed by the survival curves in Fig. 7B, mice in the saline group were the first to die successively. The survival duration for this group was merely 16 days. On the contrary, the $MPL_{(SS)}P$@SIS + X-ray + TMZ treatment notably extended the survival time of GBM-mice to 24 days, a duration significantly longer than that of G2 (18 days), G3 (19 days), G4 (20 days), G5 (21 days), and G6 (22 days). The survival rate also implied that when combined with X-ray irradiation and TMZ chemotherapy, $MPL_{(SS)}P$@SIS demonstrated the most optimal therapeutic effect and an exceptional outcome. The mice belonging to the saline group endured a rapid loss in weight due to the encroachment of GBM and the malfunctioning of the brain. Conversely, in the case of groups G6 and G7, there were absolutely no substantial alterations in their body weights. This finding firmly confirms that these particular groups are capable of effectively restraining the growth of GBM without any noticeable toxic effects or adverse side effects, as clearly shown in Fig. 7C. The growth progress of GBM was closely monitored *via* luciferin bioluminescence under the IVIS imaging system and was quantified utilizing relative bioluminescence counts. When a comparison is made with other treatment groups, it is unmistakably the treatment involving $MPL_{(SS)}P$@SIS + X-ray + TMZ that presents the strongest inhibition of the growth of GBM. This is solidly evidenced by the fact that it has the lowest bioluminescence, as vividly depicted in Fig. 7D and Supporting Information Fig. S41.

H&E staining was performed on multiple organs, including the heart, liver, spleen, lungs, and kidneys, removed from mice with different treatments (Fig. 7E, Supporting Information Fig. S42). The results demonstrated that the injection of the nanocapsules did not induce morphological changes or inflammatory responses in the organs. In addition, after treatment, the routine blood analysis of AST (Fig. 7F), ALT (Fig. 7G), BUN (Fig. 7H), and CREA (Fig. 7I) were all determined to be within the normal range of the biochemical analyses. This fact strongly suggests that, in this *in vivo* efficacy investigation, the concentration and administration times that have been utilized for the mice were relatively secure and will not bring about adverse side effects and apparent toxic effects. After the treatment, hemolysis experiments were performed (Supporting Information Fig. S43), which showed that the delivery system had good compatibility with red blood cells. Overall, these results confirmed the biocompatibility and biosafety of nanocapsules.

Post-treatment, WB analysis was performed to assess BRD4 protein expression levels in different treatment groups. As shown in Fig. 8A, the nanocapsule treatment group exhibited a significantly reduced BRD4 protein expression level compared to the control and other treatment groups,

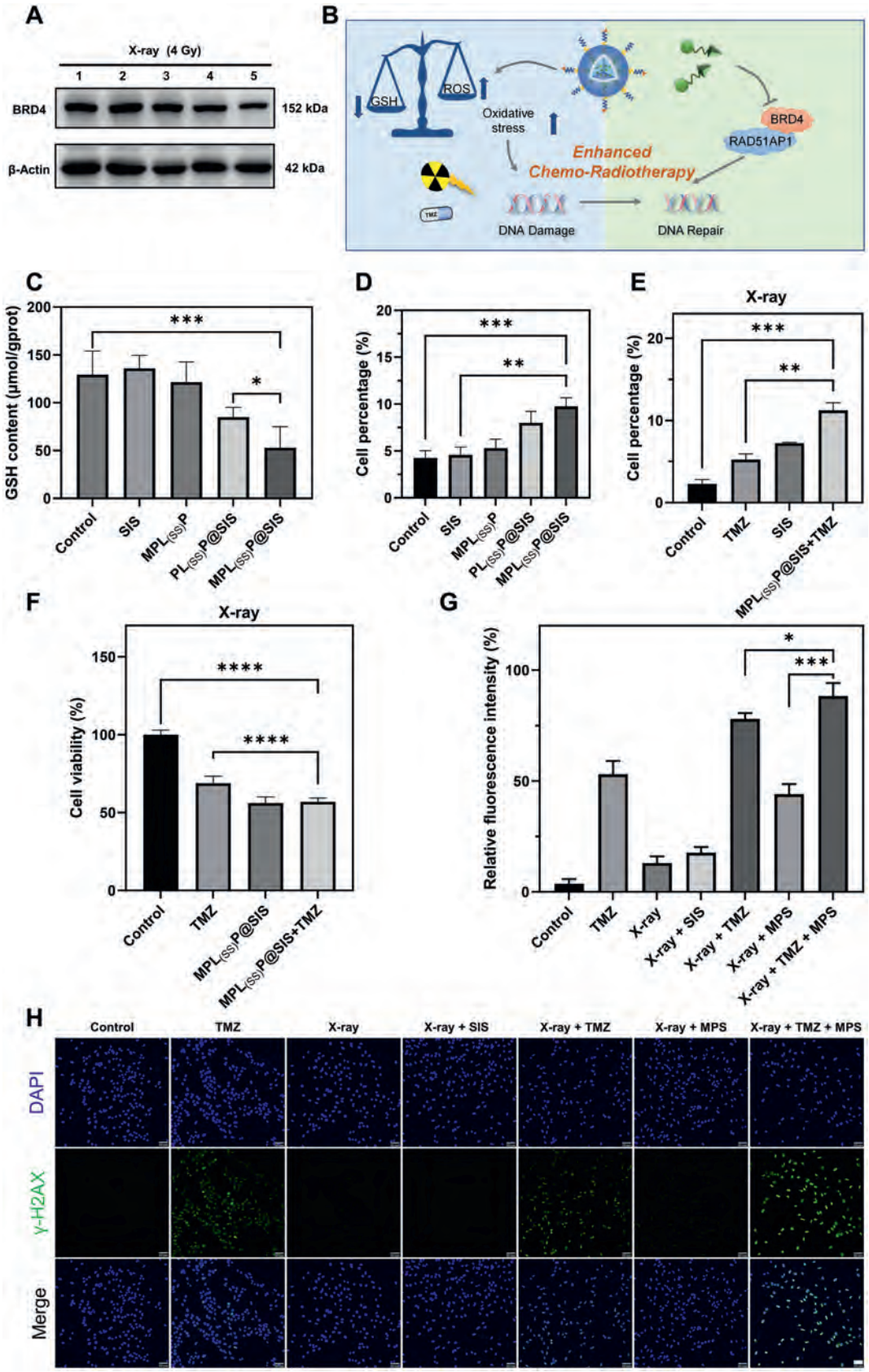

Figure 5 $MPL_{(SS)}P$@SIS nanocapsules cumulatively sensitized tumor to radio-chemotherapy. (A) WB assay of BRD4 in G422s treated with different groups accompanied by X-ray (1: X-ray, 2: X-ray + SIS, 3: X-ray + TMZ, 4: X-ray + $MPL_{(SS)}P$@SIS, 5: X-ray + TMZ + $MPL_{(SS)}P$@SIS). (B) Schematic diagram of PROTAC-integrated nanocapsules regulating oxidative stress to enhance radio-

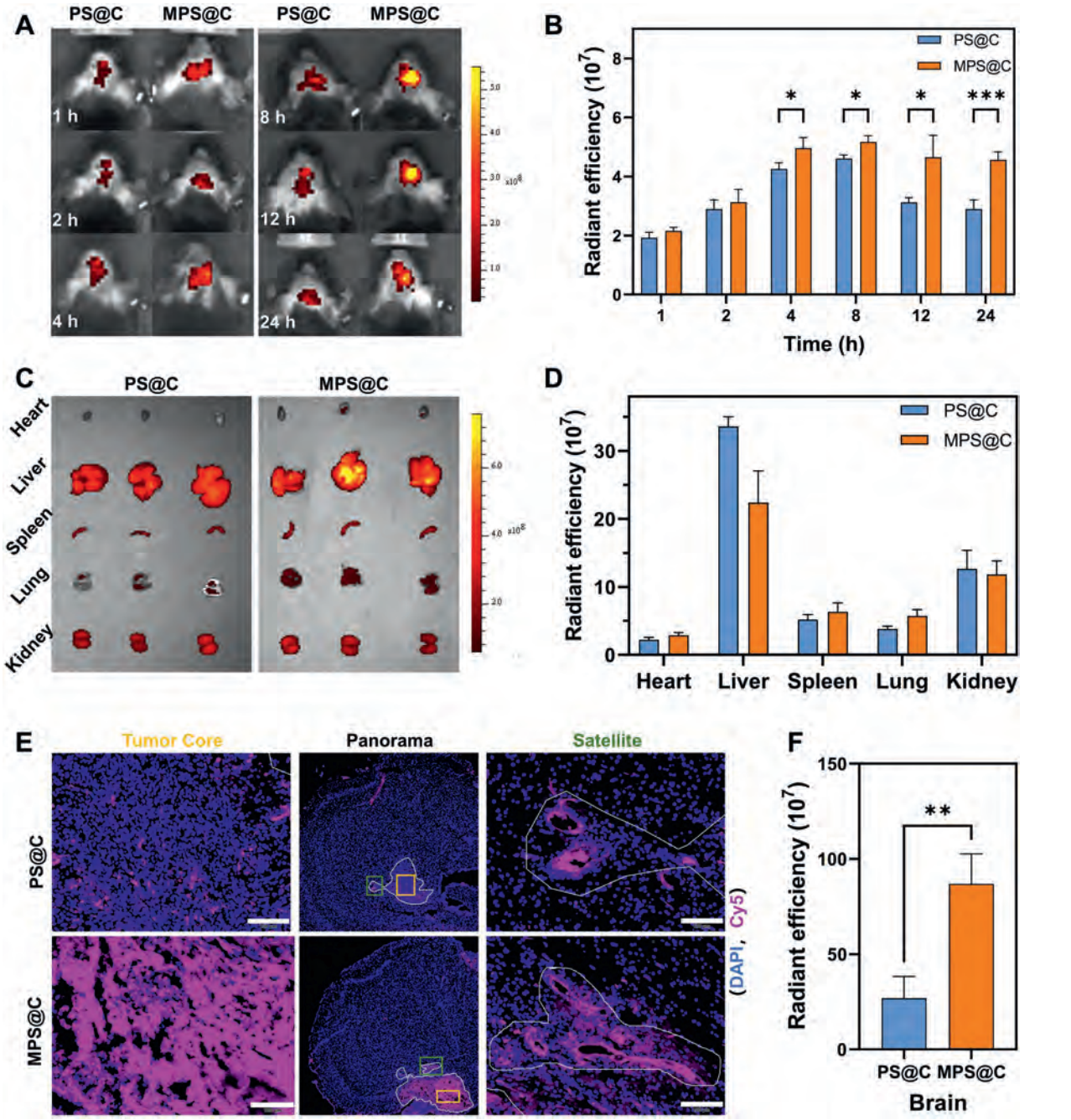

Figure 6 *In vivo* distribution and brain targeting of the nanocapsules. (A) Distribution of Cy5-labeled nanocapsules *in vivo* at different time points. (B) Quantification of (A) ($n = 3$). (C) Radiant efficiency of Cy5 fluorescence intensity in major organs 24 h post-injection. (D) Quantification of (C) ($n = 3$). (E) Representative images of the distribution of Cy5-labeled nanocapsules in the tumor section (blue: DAPI for nucleus; red: Cy5 for nanocapsules; scale bar = 100 μm). (F) Radiant efficiency of Cy5 fluorescence intensity in brains 24 h post-injection ($n = 3$). Data are presented as mean ± SD. *$P < 0.05$. ns, not significant.

particularly when combined with RT and chemotherapy. Importantly, WB analysis revealed the presence of lower molecular weight bands corresponding to ubiquitinated BRD4 degradation products (Fig. 8B), indicating that the nanocapsules induced BRD4 degradation *via* the ubiquitin−proteasome pathway.

chemotherapy effects. (C) GSH consumption in G422s treated with different groups for 24 h ($n = 3$). (D) Flow cytometry analysis of ROS probe in different groups ($n = 3$). (E) Flow cytometry analysis of ROS probe in different groups accompanied by X-ray ($n = 3$). (F) Cell viability of G422 cells treated with different groups accompanied by X-ray ($n = 3$). (G) Relative fluorescence intensity of (H) ($n = 3$). (H) Immunostaining of DNA-damaged markers in G422s treated with different groups (green: γ-H2AX; blue: DAPI; scale bar = 50 μm; MPS = $MPL_{(SS)}P$@SIS). Data are presented as mean ± SD. *$P < 0.05$. ns, not significant.

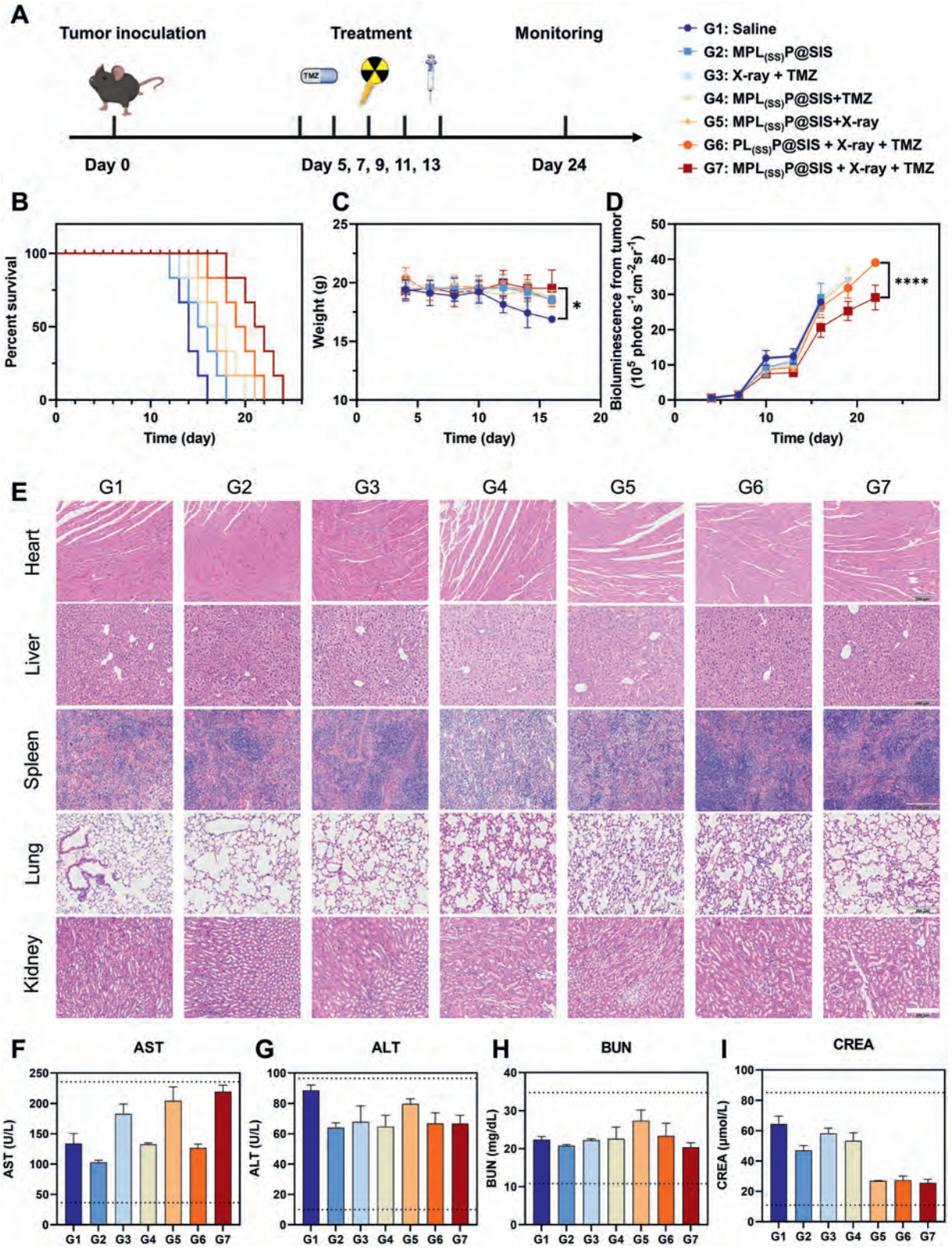

Figure 7 *In vivo* therapeutic efficacy of $MPL_{(SS)}P@SIS$. (A) Schematic diagram of the animal experimental protocol. (B) Survival rates of mice following various treatments. (C) Changes in body weight of different groups ($n = 6$). (D) Quantitative analysis of IVIS bioluminescence signals from GBM-bearing mice in different groups ($n = 6$). (E) Representative H&E results from the main organs in different groups (scale bar = 200 μm). (F–I) Biochemical analysis of serum parameters, including (F) AST, (G) ALT, (H) BUN, and (I) CREA, from blood samples collected post-treatment in different mice ($n = 3$). Data are presented as mean ± SD. $^*P < 0.05$. ns, not significant.

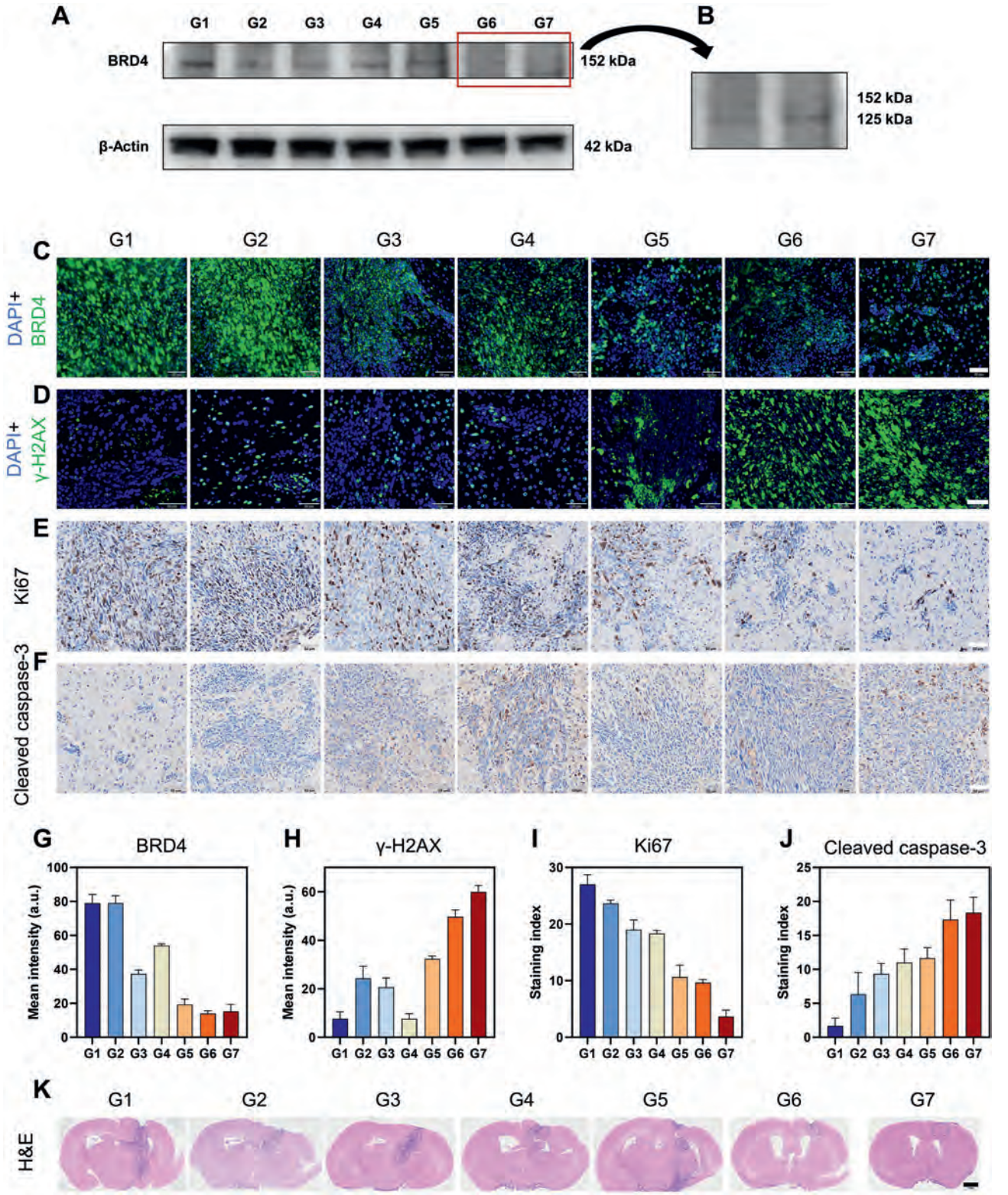

Figure 8 Enhanced therapeutic efficacy of radio-chemotherapy *in vivo*. (A)WB of BRD4 expression in GBM model mice. (B) WB of degraded BRD4. (C) Immunostaining of BRD4 in tumor slices of different groups (green: BRD4; blue: DAPI; scale bar = 50 μm). (D) Immunostaining of DNA-damaged markers in tumor slices of different groups (green: γ-H2AX; blue: DAPI; scale bar = 50 μm). (E) Ki67 and (F) Cleaved caspase-3 staining of tumor sections from GBM-bearing mice with different treatments (scale bar = 50 μm). (G) Quantitative analysis of immunofluorescence analysis of BRD4 ($n = 3$). (H) Quantitative analysis of immunofluorescence analysis of γ-H2AX ($n = 3$). (I) Quantitative analysis from Ki67 staining ($n = 3$). (J) Quantitative analysis from cleaved caspase-3 staining ($n = 3$). (K) Representative H&E staining results from the brain section of different groups (scale bar = 1 mm). Data are presented as mean ± SD. $^*P < 0.05$. ns, not significant.

The results were consistent with the immunofluorescence staining of BRD4 from tumor sections, and its subsequent quantitative analysis demonstrated a significant reduction in BRD4 expression following combined radio-chemotherapy and nanocapsule treatment (Fig. 8C). Moreover, the marked increase in the expression of the DNA damage marker γ-H2AX was observed, indicating enhanced DNA damage in GBM-bearing mice following combined radio-chemotherapy and nanocapsule treatment (Fig. 8D). Furthermore, Ki67 and cleaved caspase-3 staining were conducted on brain sections of each group to quantify the proliferation-inhibitory and apoptotic effects of different treatments (Fig. 8E and F). The immunohistochemical (IHC) assay indicated that the Ki67 signal was most intense in the saline group (G1) and least intense in the $MPL_{(SS)}$P@SIS + X-ray + TMZ group (G7). Compared to G1, the cleaved caspase-3 signal was more pronounced in the other 6 groups, with G7 exhibiting the strongest signal. Meanwhile, the quantitative analysis of BRD4 and γ-H2AX was also consistent with the above results (Fig. 8G and H). Statistical and quantitative analyses conducted using ImageJ software further indicated that the G7 group had the lowest number of Ki67-positive cells in the tumor sections (Fig. 8I). Conversely, there was a significant increase in the number of cleaved caspase-3-positive cells in this group (Fig. 8J).

The results demonstrated that the combination of $MPL_{(SS)}$P@SIS with X-rays and TMZ significantly enhanced apoptosis in GBM while also inhibiting the proliferation of GBM cells. In addition, H&E results of brain sections further validated that $MPL_{(SS)}$P@SIS alongside X-ray and TMZ group got the most effective tumor suppression *in vivo*, as these sections displayed the smallest tumor area compared to other treatment groups (Fig. 8K). Besides, the finding aligns with the bioluminescence quantification observed throughout the treatment. Overall, these results confirmed the biocompatibility and biosafety of nanocapsules. Overall, these results confirmed the $MPL_{(SS)}$P@SIS nanocapsules, alongside the X-ray and TMZ group, got the most effective tumor suppression *in vivo*.

4. Conclusions

In summary, the nanocapsules designed to degrade BRD4 following radio-chemotherapy significantly enhance the efficacy of anti-GBM treatment. The $MPL_{(SS)}$P@SIS nanocapsules, composed of SIS, GSH-responsive materials and surface-modified with MLT, were constructed to address the challenges of resistance and poor prognosis associated with conventional radio-chemotherapy for GBM. These nanocapsules effectively penetrate the BBB and selectively target the GBM site *via* LAT1 transporters. Upon reaching the tumor microenvironment, the SIS is released in response to GSH, increasing ROS levels. The elevated ROS, generated through the breaking of disulfide bonds in the nanocapsules, facilitates direct DNA damage during radiotherapy. Concurrently, the PROTACs promote BRD4 degradation through the ubiquitin−proteasome system, thereby inhibiting the DNA damage repair processes. In addition, the SIS, released from $MPL_{(SS)}$P@SIS nanocapsules break the BRD4−RAD51AP1 axis to enhance radiosensitivity, and have a synergistic effect in combination with TMZ for anti-tumor effects. Consequently, as the nanosensitizer, $MPL_{(SS)}$P@SIS effectively amplifies DNA damage, enhancing the therapeutic efficacy of radio-chemotherapy. In conclusion, the $MPL_{(SS)}$P@SIS nanocapsules achieve precise drug delivery to intracranial GBMs, resulting in high therapeutic efficiency with minimal side effects.

Acknowledgments

The authors acknowledge the support from the National Key R&D Program of China (2023YFC3404103), National Natural Science Foundation of China (82473853, 82361148716), Shanghai Municipal Science and Technology Commission Intergovernmental Cooperation Project (24430710700, China), Shanghai Natural Science Foundation Project (22ZR1414100, China), Shanghai Municipal Science and Technology Major Project (Grant 2018SHZDZX01, China) and ZJLab.

Author contributions

Yun Guo and Tao Sun contributed to design, concept, and supervise the project; Yun Guo, Haoyu You and Zheng Zhou performed the synthesis and characterization of the polymers and nanoparticles; Yunke Bi and Chen Jiang provided valuable advice for article writing; Mingzhu Fang and Shilin Zhang constructed animal models; Zonghua Tian wrote the manuscript; Yun Chen and Jingyi Zhou revised and edited the manuscript; Xiaobao Yang synthesised SIAIS171142 compounds. All authors have approved the final article.

Conflicts of interest

The authors declare that they have no competing financial interests or personal relationships that could have appeared to influence the work reported in this paper.

Appendix A. Supporting information

Supporting information to this article can be found online at https://doi.org/10.1016/j.apsb.2025.03.018.

References

1. Tan AC, Ashley DM, Lopez GY, Malinzak M, Friedman HS, Khasraw M. Management of glioblastoma: state of the art and future directions. *CA Cancer J Clin* 2020;**70**:299−312.
2. Ostrom QT, Patil N, Cioffi G, Waite K, Kruchko C, Barnholtz-Sloan JS. CBTRUS statistical report: primary brain and other central nervous system tumors diagnosed in the United States in 2013−2017. *Neuro Oncol* 2020;**22**:iv1−96.
3. Qazi MA, Vora P, Venugopal C, Sidhu SS, Moffat J, Swanton C, et al. Intratumoral heterogeneity: pathways to treatment resistance and relapse in human glioblastoma. *Ann Oncol* 2017;**28**:1448−56.
4. Lee SY. Temozolomide resistance in glioblastoma multiforme. *Genes Dis* 2016;**3**:198−210.
5. Shergalis A, Bankhead 3rd A, Luesakul U, Muangsin N, Neamati N. Current challenges and opportunities in treating glioblastoma. *Pharmacol Rev* 2018;**70**:412−45.
6. Qi D, Li J, Quarles CC, Fonkem E, Wu E. Assessment and prediction of glioblastoma therapy response: challenges and opportunities. *Brain* 2023;**146**:1281−98.
7. Vignard J, Mirey G, Salles B. Ionizing-radiation induced DNA double-strand breaks: a direct and indirect lighting up. *Radiother Oncol* 2013; **108**:362−9.
8. Strobel H, Baisch T, Fitzel R, Schilberg K, Siegelin MD, Karpel-Massler G, et al. Temozolomide and other alkylating agents in glioblastoma therapy. *Biomedicines* 2019;**7**:69.

9. Petroni G, Cantley LC, Santambrogio L, Formenti SC, Galluzzi L. Radiotherapy as a tool to elicit clinically actionable signalling pathways in cancer. *Nat Rev Clin Oncol* 2022;**19**:114−31.
10. Johannessen TC, Bjerkvig R, Tysnes BB. DNA repair and cancer stem-like cells–potential partners in glioma drug resistance?. *Cancer Treat Rev* 2008;**34**:558−67.
11. Kelley MR, Fishel ML. DNA repair proteins as molecular targets for cancer therapeutics. *Anticancer Agents Med Chem* 2008;**8**:417−25.
12. Zhang D, Tang B, Xie X, Xiao YF, Yang SM, Zhang JW. The interplay between DNA repair and autophagy in cancer therapy. *Cancer Biol Ther* 2015;**16**:1005−13.
13. Kanzawa T, Bedwell J, Kondo Y, Kondo S, Germano IM. Inhibition of DNA repair for sensitizing resistant glioma cells to temozolomide. *J Neurosurg* 2003;**99**:1047−52.
14. Huang RX, Zhou PK. DNA damage response signaling pathways and targets for radiotherapy sensitization in cancer. *Signal Transduct Target Ther* 2020;**5**:60.
15. Chen L, Gai X, Yu X. Pre-rRNA facilitates the recruitment of RAD51AP1 to DNA double-strand breaks. *J Biol Chem* 2024;**300**:107115.
16. Zhang S, Lai Y, Pan J, Saeed M, Li S, Zhou H, et al. PROTAC prodrug-integrated nanosensitizer for potentiating radiation therapy of cancer. *Adv Mater* 2024;**36**:e2314132.
17. Fu Y, Yang B, Cui Y, Hu X, Li X, Lu F, et al. BRD4 inhibition impairs DNA mismatch repair, induces mismatch repair mutation signatures and creates therapeutic vulnerability to immune checkpoint blockade in MMR-proficient tumors. *J Immunother Cancer* 2023;**11**:e006070.
18. Dhalluin C, Carlson JE, Zeng L, He C, Aggarwal AK, Zhou MM. Structure and ligand of a histone acetyltransferase bromodomain. *Nature* 1999;**399**:491−6.
19. Wu SY, Chiang CM. The double bromodomain-containing chromatin adaptor Brd4 and transcriptional regulation. *J Biol Chem* 2007;**282**: 13141−5.
20. Moriniere J, Rousseaux S, Steuerwald U, Soler-Lopez M, Curtet S, Vitte AL, et al. Cooperative binding of two acetylation marks on a histone tail by a single bromodomain. *Nature* 2009;**461**:664−8.
21. Donati B, Lorenzini E, Ciarrocchi A. BRD4 and Cancer: going beyond transcriptional regulation. *Mol Cancer* 2018;**17**:164.
22. Duan W, Yu M, Chen J. BRD4: new hope in the battle against glioblastoma. *Pharmacol Res* 2023;**191**:106767.
23. Ye Y, Zhong W, Qian J, Zhang J, Xu T, Han R, et al. Comprehensive analysis of the prognosis and immune infiltrates for the BET protein family reveals the significance of BRD4 in glioblastoma multiforme. *Front Cell Dev Biol* 2023;**11**:1042490.
24. Lu J, Qian Y, Altieri M, Dong H, Wang J, Raina K, et al. Hijacking the E3 ubiquitin ligase cereblon to efficiently target BRD4. *Chem Biol* 2015;**22**:755−63.
25. Filippakopoulos P, Qi J, Picaud S, Shen Y, Smith WB, Fedorov O, et al. Selective inhibition of BET bromodomains. *Nature* 2010;**468**: 1067−73.
26. Li K, Crews CM. PROTACs: past, present and future. *Chem Soc Rev* 2022;**51**:5214−36.
27. Li X, Song Y. Proteolysis-targeting chimera (PROTAC) for targeted protein degradation and cancer therapy. *J Hematol Oncol* 2020;**13**:50.
28. Nalawansha DA, Crews CM. PROTACs: an emerging therapeutic modality in precision medicine. *Cell Chem Biol* 2020;**27**:998−1014.
29. Zhang C, Zeng Z, Cui D, He S, Jiang Y, Li J, et al. Semiconducting polymer nano-PROTACs for activatable photo-immunometabolic cancer therapy. *Nat Commun* 2021;**12**:2934.
30. Chirnomas D, Hornberger KR, Crews CM. Protein degraders enter the clinic—a new approach to cancer therapy. *Nat Rev Clin Oncol* 2023; **20**:265−78.
31. Li M, Zhi Y, Liu B, Yao Q. Advancing strategies for proteolysis-targeting chimera design. *J Med Chem* 2023;**66**:2308−29.
32. Parkin HC, Shopperly LK, Perez MR, Willerth SM, Manners I. Uniform block copolymer nanofibers for the delivery of paclitaxel in 2D and 3D glioblastoma tumor models. *Biomater Sci* 2024;**12**:5283−94.
33. Zhan J, Li X, Mu Y, Yao H, Zhu JJ, Zhang J. A photoactivatable upconverting nanodevice boosts the lysosomal escape of PROTAC degraders for enhanced combination therapy. *Biomater Sci* 2024;**12**: 3686−99.
34. Chen J, Qiu M, Ma F, Yang L, Glass Z, Xu Q. Enhanced protein degradation by intracellular delivery of pre-fused PROTACs using lipid-like nanoparticles. *J Control Release* 2021;**330**:1244−9.
35. Saraswat AL, Vartak R, Hegazy R, Patel A, Patel K. Drug delivery challenges and formulation aspects of proteolysis targeting chimera (PROTACs). *Drug Discov Today* 2023;**28**:103387.
36. Zeng S, Huang W, Zheng X, Liyan C, Zhang Z, Wang J, et al. Proteolysis targeting chimera (PROTAC) in drug discovery paradigm: recent progress and future challenges. *Eur J Med Chem* 2021;**210**: 112981.
37. Wang Y, Han L, Liu F, Yang F, Jiang X, Sun H, et al. Targeted degradation of anaplastic lymphoma kinase by gold nanoparticle-based multi-headed proteolysis targeting chimeras. *Colloids Surf B Biointerfaces* 2020;**188**:110795.
38. Zhou Z, Li K, Guo Y, Liu P, Chen Q, Fan H, et al. ROS/electro dual-reactive nanogel for targeting epileptic foci to remodel aberrant circuits and inflammatory microenvironment. *ACS Nano* 2023;**17**: 7847−64.
39. Rautio J, Gynther M, Laine K. LAT1-mediated prodrug uptake: a way to breach the blood−brain barrier?. *Ther Deliv* 2013;**4**:281−4.
40. Ji WO, Lee MH, Kim GH, Kim EH. Quantitation of the ROS production in plasma and radiation treatments of biotargets. *Sci Rep* 2019; **9**:19837.
41. Guo L, Zhang D. Cyclic poly(alpha-peptoid)s and their block copolymers from N-heterocyclic carbene-mediated ring-opening polymerizations of *N*-substituted *N*-carboxylanhydrides. *J Am Chem Soc* 2009;**131**:18072−4.
42. Wei Y, Sun Y, Wei J, Qiu X, Meng F, Storm G, et al. Selective transferrin coating as a facile strategy to fabricate BBB-permeable and targeted vesicles for potent RNAi therapy of brain metastatic breast cancer *in vivo*. *J Control Release* 2021;**337**:521−9.
43. Han L, Jiang C. Evolution of blood−brain barrier in brain diseases and related systemic nanoscale brain-targeting drug delivery strategies. *Acta Pharm Sin B* 2021;**11**:2306−25.
44. Venkateswaran N, Garcia R, Lafita-Navarro MC, Hao YH, Perez-Castro L, Nogueira PAS, et al. Tryptophan fuels MYC-dependent liver tumorigenesis through indole 3-pyruvate synthesis. *Nat Commun* 2024;**15**:4266.
45. Sadik A, Somarribas Patterson LF, Ozturk S, Mohapatra SR, Panitz V, Secker PF, et al. IL4I1 Is a Metabolic immune checkpoint that activates the AHR and promotes tumor progression. *Cell* 2020;**182**:1252.
46. Platten M, Weller M, Wick W. Shaping the glioma immune microenvironment through tryptophan metabolism. *CNS Oncol* 2012;**1**: 99−106.
47. Alkonyi B, Mittal S, Zitron I, Chugani DC, Kupsky WJ, Muzik O, et al. Increased tryptophan transport in epileptogenic dysembryoplastic neuroepithelial tumors. *J Neuro Oncol* 2012;**107**:365−72.
48. Gonzalez-Carter DA, Ong ZY, McGilvery CM, Dunlop IE, Dexter DT, Porter AE. L-DOPA functionalized, multi-branched gold nanoparticles as brain-targeted nano-vehicles. *Nanomedicine* 2019;**15**:1−11.
49. Wang Z, Chi D, Wu X, Wang Y, Lin X, Xu Z, et al. Tyrosine modified irinotecan-loaded liposomes capable of simultaneously targeting LAT1 and $ATB^{0,+}$ for efficient tumor therapy. *J Control Release* 2019; **316**:22−33.
50. Vyas A, Jain A, Hurkat P, Jain A, Jain SK. Targeting of AIDS related encephalopathy using phenylalanine anchored lipidic nanocarrier. *Colloids Surf B Biointerfaces* 2015;**131**:155−61.
51. Nass RD, Wagner M, Surges R, Holdenrieder S. Time courses of HMGB1 and other inflammatory markers after generalized convulsive seizures. *Epilepsy Res* 2020;**162**:106301.
52. Zhao J, Ye Z, Yang J, Zhang Q, Shan W, Wang X, et al. Nanocage encapsulation improves antiepileptic efficiency of phenytoin. *Biomaterials* 2020;**240**:119849.
53. Wu Z, Hofman FM, Zlokovic BV. A simple method for isolation and characterization of mouse brain microvascular endothelial cells. *J Neurosci Methods* 2003;**130**:53−63.

54. Du C, Wang J, Liu X, Li H, Geng D, Yu L, et al. Construction of pepstatin A-conjugated ultrasmall SPIONs for targeted positive MR imaging of epilepsy-overexpressed p-glycoprotein. *Biomaterials* 2020;**230**:119581.
55. Yuan W, Lv Y, Zeng M, Fu BM. Non-invasive measurement of solute permeability in cerebral microvessels of the rat. *Microvasc Res* 2009; **77**:166−73.
56. Li X, Pu W, Zheng Q, Ai M, Chen S, Peng Y. Proteolysis-targeting chimeras (PROTACs) in cancer therapy. *Mol Cancer* 2022;**21**:99.
57. Loven J, Hoke HA, Lin CY, Lau A, Orlando DA, Vakoc CR, et al. Selective inhibition of tumor oncogenes by disruption of super-enhancers. *Cell* 2013;**153**:320−34.
58. Delmore JE, Issa GC, Lemieux ME, Rahl PB, Shi J, Jacobs HM, et al. BET bromodomain inhibition as a therapeutic strategy to target c-Myc. *Cell* 2011;**146**:904−17.
59. Schultz DR, Harrington Jr WJ. Apoptosis: programmed cell death at a molecular level. *Semin Arthritis Rheum* 2003;**32**:345−69.
60. Zhang H, Nimmer PM, Tahir SK, Chen J, Fryer RM, Hahn KR, et al. Bcl-2 family proteins are essential for platelet survival. *Cell Death Differ* 2007;**14**:943−51.
61. Dong Y, Zhang D, Cai M, Luo Z, Zhu Y, Gong L, et al. SPOP regulates the DNA damage response and lung adenocarcinoma cell response to radiation. *Am J Cancer Res* 2019;**9**:1469−83.
62. Gao Z, Xu J, Fan Y, Qi Y, Wang S, Zhao S, et al. PDIA3P1 promotes temozolomide resistance in glioblastoma by inhibiting C/EBPβ degradation to facilitate proneural-to-mesenchymal transition. *J Exp Clin Cancer Res* 2022;**41**:223.
63. Ballesteros-Zebadua P, Chavarria A, Celis MA, Paz C, Franco-Perez J. Radiation-induced neuroinflammation and radiation somnolence syndrome. *CNS Neurol Disord Drug Targets* 2012;**11**:937−49.
64. Birch-Machin MA, Russell EV, Latimer JA. Mitochondrial DNA damage as a biomarker for ultraviolet radiation exposure and oxidative stress. *Br J Dermatol* 2013;**169**(Suppl 2):9−14.